

¹

José D. Ruiz-Álvarez

²

Compiled on 23/05/2015 at 17:13

1 The CMS experiment at LHC

The CMS experiment is one of the biggest particle physics experiments on the world. It is located at the ring of the LHC that is the main accelerator managed by CERN, the European Organization for Nuclear Research or Centre Européen pour la Recherche Nucléaire by its french name. This center constitutes the biggest center for research on particle physics all over the world. All along its 60 years of existence, from 1954, 21 member states have been joining it, but an overall of 113 countries participate in different ways on this center.

On the present chapter we discuss in detail different aspects of the LHC accelerator and the CMS experiment. In particular we make some emphasis in the CMS sub-detectors related to jets, objects that play the main role on the search that is the main subject of the present work. We also discuss the present state of both machines, their achievements and the challenges that were overcome. Finally, also the expectations and goals for the upcoming run II are mentioned.

1.1 The Large Hadron Collider

The Large Hadron Collider, or LHC [1], is a machine that accelerates and collides protons and lead. This machine is the biggest particle collider nowadays with a circumference of 27 km. It also achieves the highest energy by a collider up to present, planned to be 14 TeV at the center of mass of the collision. On the first run of the machine only 8 TeV were achieved, and next run is planned to start with 13 TeV. It's located in French-Swiss border near to Geneva. The tunnel for the machine was carved around 100 m under the ground, 45 m under the Jura mountains and 170 m under the Léman lake with an inclination of around 1.4%, sloping down towards the lake . This machine has used as much as possible old LEP buildings and sites, that was an electron-positron collider built between 1984 and 1989.

The protons and heavy ions accelerated by the machine collide in different points where dedicated experiments are located to detect and study the product from the collisions. The four main experiments located on the LHC ring are CMS [2, 3], ATLAS [4], LHCb [5] and ALICE [6]. The first two are experiments of generic purpose where searches for new physics and also precision measurements are performed. LHCb is dedicated to the physics of the b-quark, and ALICE focuses on

37 the study of the quark-gluon plasma produced from heavy ions collisions. Even if
38 one of the principal objectives of the construction of the LHC was the search for
39 the Higgs boson, generic searches on new physics have been conducted from the
40 very beginning of the first data taking in 2009. Moreover, after the Higgs discov-
41 ery in 2012 there is a growing effort on the searches for new physics and precision
42 measurement of the properties of the Higgs.

43 The LHC is a complex machine composed of several parts. The two principal
44 parts are the injector chain and the main ring. A diagram of the whole CERN
45 complex can be seen in figure 1.1. The injector chain has different stages that
46 pre-accelerate protons and heavy ions to be injected into the main ring of LHC.

47 **1.1.1 Injector chain**

48 The injector chain begins with the proton source. Protons are extracted via ioniza-
49 tion of Hydrogen gas in the Duoplasmatron Proton Ion Source. Such extraction is
50 pulsed, what makes up the first bunch structure. The extracted protons are then
51 accelerated up to 50 MeV in the linear accelerator, Linac2, that dates from 1978.
52 After this first stage several steps are followed:

- 53 1. Linac2 injects proton bunches in the Proton Synchrotron Booster (PSB)
54 where they are accelerated to 1.4 GeV.
- 55 2. From PSB, the protons are delivered to the Proton Synchrotron (PS) where
56 they reach an energy of 25 GeV. In the PS the bunches are also split from 6
57 initial bunches to 72 spaced by 25 ns.
- 58 3. Finally, the pre-acceleration chain is finished by the SPS, Super Proton Syn-
59 chrotron. There the bunches are accelerated up to 450 GeV right before
60 being inserted into the main LHC ring.

61 The whole pre-acceleration chain has been optimized to obtain the best possible
62 performance on the final acceleration in the LHC main ring. All parameters are
63 carefully controlled, for example the number of bunches, the separation between
64 bunches, the separation between trains of bunches or the injection energy to each
65 subsystem. It's also remarkable to notice the level of control achieved in the
66 bunches manipulation, from old subsystems as the PS from 1959 or the newest,
67 the SPS that dates from 1976.

68 Some recent plans for future accelerator have been studied using the LHC main
69 ring as injector for a bigger accelerator, for example the so called FCC (Future Cir-
70 cular Collider) at CERN. The FCC could be built perform proton-proton, electron-
71 positron or electron-proton collisions, versions that are called respectively FCC-hh,
72 FCC-ee and FCC-he. The FCC-hh is being designed to achieve 100 TeV of center
73 of mass energy in a tunnel of 80-100 km of circumference.

CERN Accelerator Complex

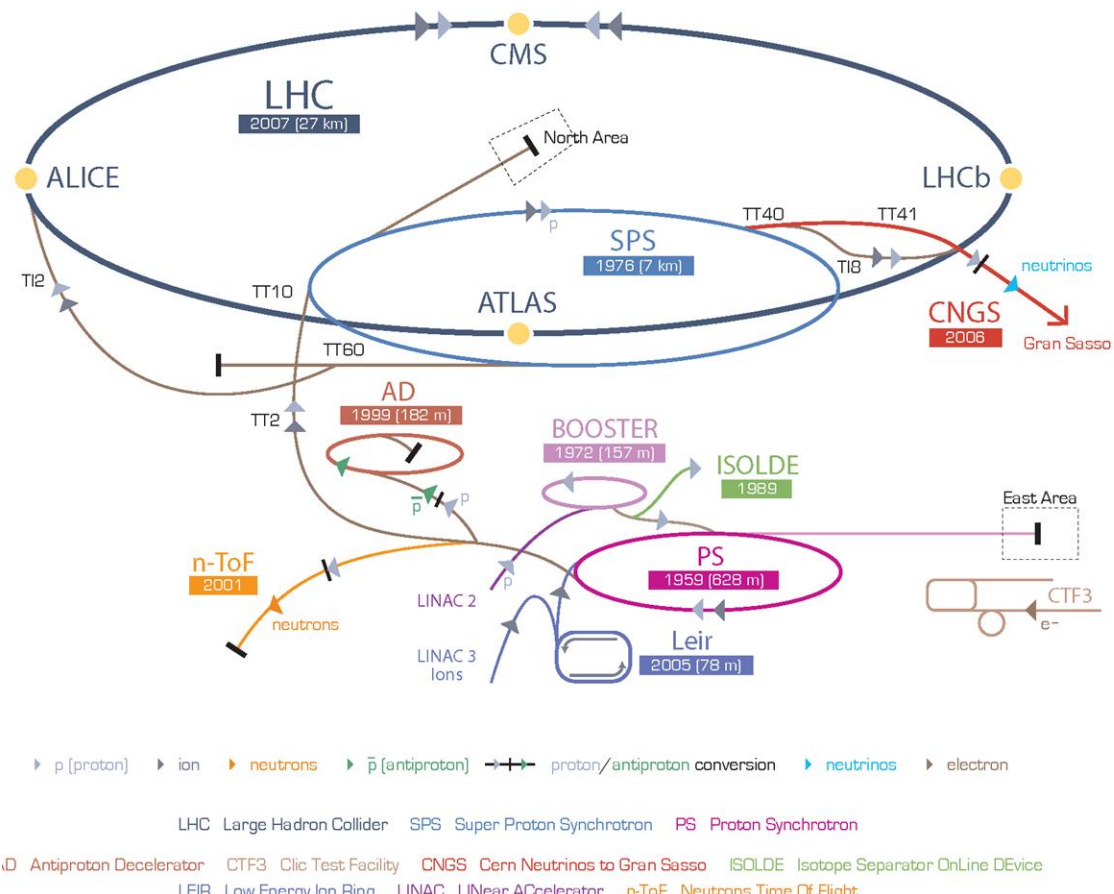


Figure 1.1: Organization of CERN accelerator complex

⁷⁴ **1.1.2 Main ring**

⁷⁵ The main ring is composed of two rings that accelerate the proton bunches in
⁷⁶ opposite directions, clock-wise and counter clock-wise. An schematic view of the
⁷⁷ design of the main ring can be seen in figure 1.2. The rings crosses in different
⁷⁸ points in order to collide the protons and they are divided in eight straight sections
⁷⁹ and eight arcs. In each octant bunches are controlled by dipole magnets. These
⁸⁰ complex magnets, in figure 1.3, need to produce a very strong magnetic field in
⁸¹ order to be able to bend a 7 TeV beam of protons. This intense magnetic field, 8.33
⁸² T, in opposite directions, is produced by electrical currents that are only achievable
⁸³ by means of superconductivity. All the 1232 dipoles operate at a temperature of
⁸⁴ 1.9 K, under cooling by liquid helium. They also operate under ultra-high-vacuum.
⁸⁵ The beam lines with a pressure less than 10^{-9} mbar and the whole dipole system
⁸⁶ with 10^{-6} mbar, that serves also as insulating system from the surroundings. In
⁸⁷ addition, the LHC main ring has other magnets that focus and correct different
⁸⁸ characteristics of the beam: 520 quadrupoles, 2464 sextupoles, 1232 octupoles.

⁸⁹ **Luminosity**

⁹⁰ In collider physics, such as the LHC, the figure of merit is the luminosity, given in
⁹¹ equation 1.1. The number of events per second is proportional to the luminosity,
⁹² hence is the quantity to be maximized by the design and operation of the acceler-
⁹³ ator. The collider characteristics depend on the number of bunches in the ring n_b ,
⁹⁴ the number of protons per bunch N_b , the revolution frequency f_{rev} , the relativistic
⁹⁵ gamma factor γ , the normalized rms transverse beam emittance ϵ_n and the beta
⁹⁶ function at the interaction point β^* . The denominator on 1.1 can also be rewritten
⁹⁷ in terms of the horizontal and vertical width of the bunches at the crossing, σ_x^*
⁹⁸ and σ_y^* . In addition, there is the geometric reduction factor (R) that introduces
⁹⁹ a dependence on the crossing angle of the bunches at the interaction points. In
¹⁰⁰ table 1.1.2 can be found the LHC beam parameters at injection and collision.

$$L = \frac{n_b N_b^2 f_{rev} \gamma}{4\pi \epsilon_n \beta^*} R = \frac{n_b N_b^2 f_{rev}}{4\pi \sigma_x^* \sigma_y^*} R \quad (1.1)$$

¹⁰¹ At the crossing points, the number of events coming from collisions and produced
¹⁰² via a specific process, is directly proportional to the luminosity provided by the
¹⁰³ collider, as in equation 1.1.

$$N_{events} = L \sigma_{process} \quad (1.2)$$

¹⁰⁴ where $\sigma_{process}$ is the cross section of the process.

¹⁰⁵ The total cross section of a proton-proton collision from the crossing of two
¹⁰⁶ bunches at 14 TeV is 100-110 mb [7], from three different scattering processes:

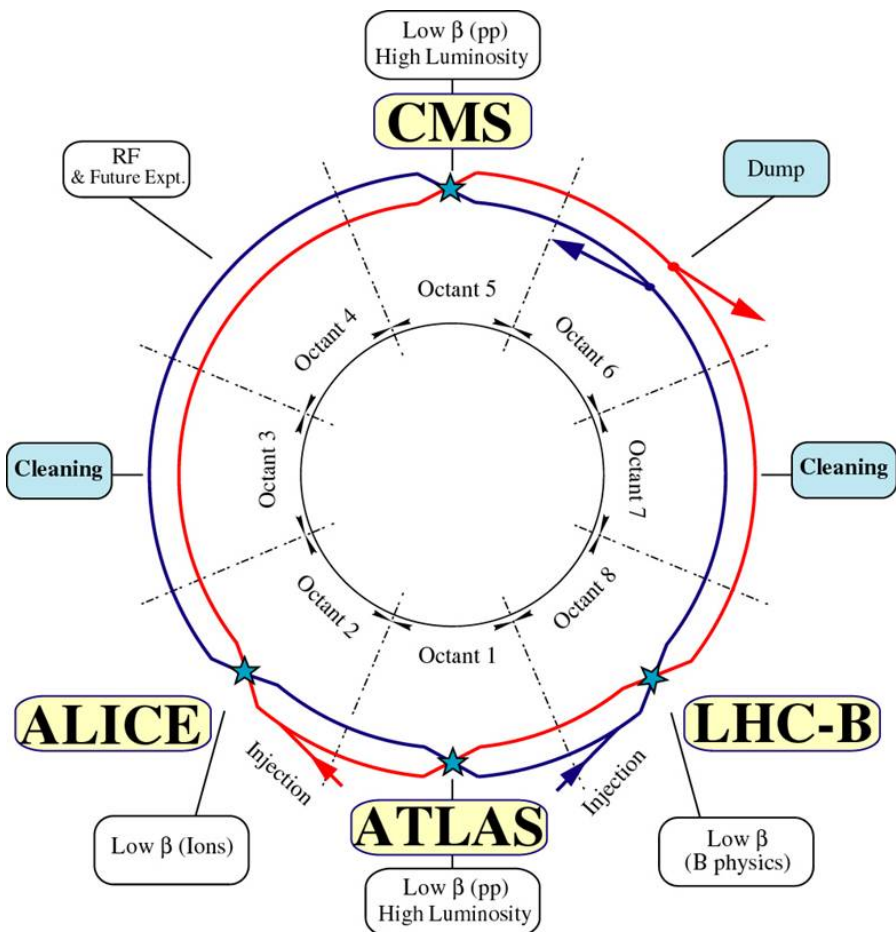


Figure 1.2: Schematic of the LHC main ring design.

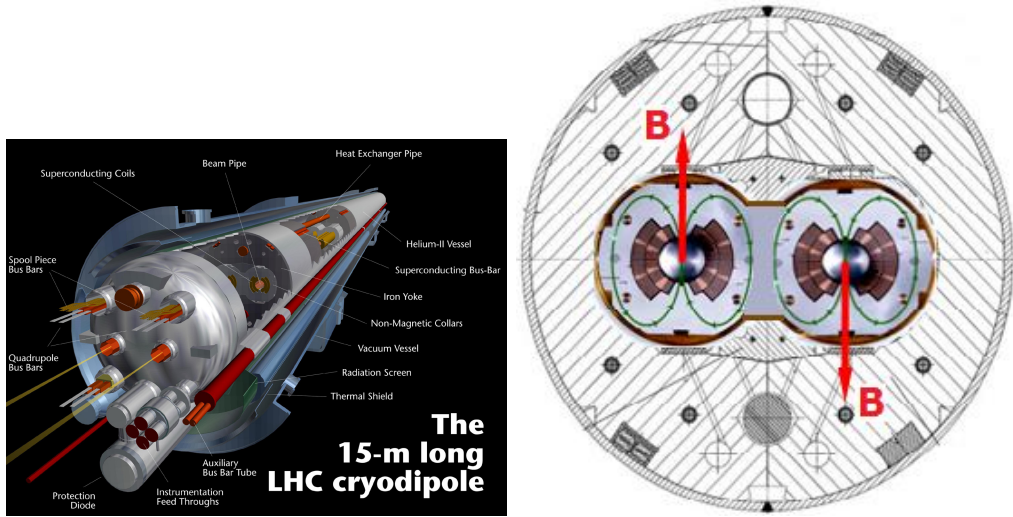


Figure 1.3: Design of LHC cryodipole and the magnetic field that bends the beam in the main ring.

elastic, diffractive and inelastic. In the elastic scattering the protons only exchange momenta but their structure remain unchanged, that is the case for the majority of collisions. In diffractive scattering momenta is exchanged and also new particles are produced in addition to the two final protons. Finally, in inelastic scattering, the constituents of the protons, the partons, interchange a big amount of momentum and produce a large quantity of particles. The inelastic processes contribute less than diffraction to the total cross section. While inelastic collisions produce particles in the central rapidity (defined in 1.2.1) region, diffractive and elastic final products have a large rapidity. Only in the hard interactions, inelastic scattering, color is exchanged, being the reason to fill up the central rapidity

Parameter/units	Injection	Collision
Energy [GeV]	450	7000
Luminosity [$\text{cm}^{-2}\text{s}^{-1}$]		10^{34}
k_b Number of bunches		2808
Bunch spacing [ns]		24.95
N_b intensity per bunch [protons/bunch]		1.15×10^{11}
Beam current [A]		0.58
ϵ_n normalized rms transverse beam emittance [μm]	3.5	3.75
f_{rev} revolution frequency [kHz]		11.25

117 region.

118 From the crossing of two bunches not only one proton-proton interaction is
119 expected. In average, 25 interactions are expected for each crossing. From them,
120 only one is coming from an inelastic collision, that is the type of process of more
121 interest for detectors as CMS or ATLAS. This fact puts an additional difficulty
122 to the detectors in order to extract the hard interaction from all the elastic and
123 diffractive collisions happening at same time. Such phenomena is known as Pile-
124 Up, an illustration of a collision with high pile-up can be found on figure 1.4 as
125 seen by the CMS detector.

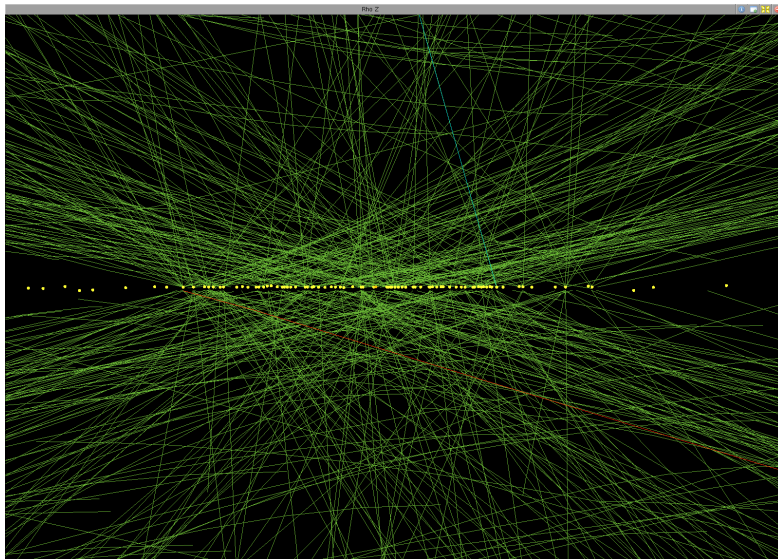


Figure 1.4: High pile-up event (78 interactions) seen by CMS detector. Event 35655522, from 198609 run, lumi 56, recorded on 2012. Image credit: Andre Holzner ©CERN

126 1.1.3 Run 1

127 On February 10 of 2013 the first stable run of the LHC reached an end. This run,
128 now called Run 1, started on November 20 of 2009. LHC was originally planned
129 to start in 2008, but an incident on one of the electric connections of one of the
130 magnets forced to stop on the 19th of September of the same year. From the
131 restart in 2009, the energy was augmented from 450 GeV to 4 TeV per beam. The
132 23th of September 2009 the first collisions were detected by the experiments. One
133 week after, the achieved center of mass energy was $\sqrt{s} = 2.36$ TeV, already higher
134 than Tevatron (0.98 TeV).

135 In 2010, from 30th March to 6th December 3.5 TeV per beam were reached de-
136 livering near 50 pb^{-1} . With the same energy, approximately 6 fb^{-1} were delivered
137 in 2011.

138 In 2012, the center of mass energy reached one additional TeV, $\sqrt{s} = 8 \text{ TeV}$,
139 and around 20 fb^{-1} of integrated luminosity were delivered between April and
140 December. On figure 1.5 can be seen the progress of the recorded luminosity by
141 CMS for 2010-2012 period. The first six weeks of 2013 were devoted to proton-lead
142 collisions.

143 After this very successful run, the LHC has been stopped for more than a year
144 for repair and maintenance of different systems in the experiments and in the LHC
145 itself to achieve higher energies. After this period, known as Long Shutdown or
146 LS1, the LHC is planned to restart a new run on the early spring of 2015.

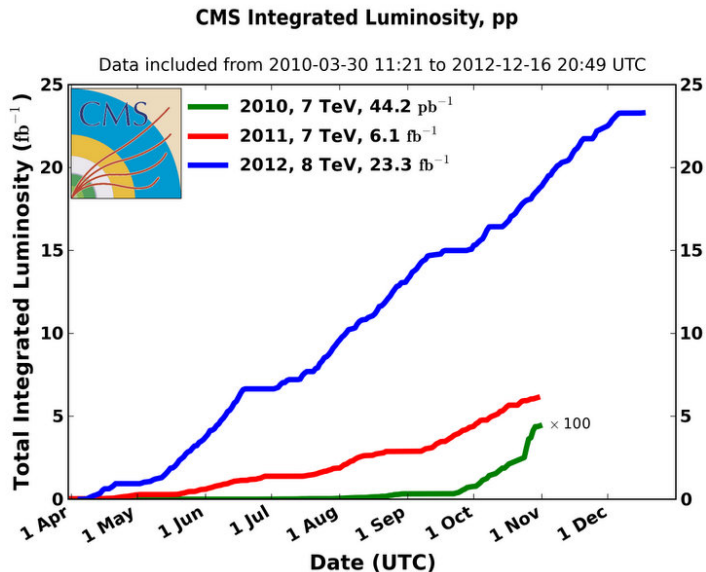


Figure 1.5: CMS integrated luminosity for proton-proton collisions delivered by LHC. ©CERN

147 1.1.4 Other experiments at LHC

148 On the main ring there are several experiments depending on the collisions de-
149 livered by the LHC main ring. The biggest are CMS [2] and ATLAS [4], both
150 of them generalist experiments designed to do precision measurements as well as
151 new physics searches. Mainly recording proton-proton collisions, they have also

152 recorded lead-lead and proton-lead collisions during the run 1. Both of them were
153 designed for high instantaneous luminosity, $L = 10^{34} \text{cm}^2\text{s}^{-1}$.

154 In addition, there are two other experiments designed for specific purposes. The
155 LHCb [5] that focus on the study of the physics of the b-hadrons, specially related
156 to the CP violation, and ALICE [6] built for the study of strongly interacting matter.
157 The first of them record proton-proton collisions at an instantaneous luminosity
158 of $10^{32} \text{cm}^2\text{s}^{-1}$ and the second record ion-ion collision with $L = 10^{27} \text{cm}^2\text{s}^{-1}$.

159 The CMS experiment is going to be described in detail in section 1.2. In the
160 following sections we are going to present very briefly the other three experiments
161 mentioned above.

162 **ATLAS**

163 The ATLAS experiment (A Toroidal LHC ApparatuS) is the biggest LHC experiment.
164 It's located at point one, as displayed on figure 1.2, on the LHC main ring.
165 It's a cylindrical detector similar to CMS, about 45 meter long, 25 meter high, and
166 weights around 7000 tons. ATLAS main components are, from inside to outside, a
167 tracking system, an electromagnetic calorimeter, a hadron calorimeter and muon
168 chambers. In between these subsystems there is an internal solenoidal magnet and
169 a set of external toroidal magnets. The detector design is presented on figure 1.6.

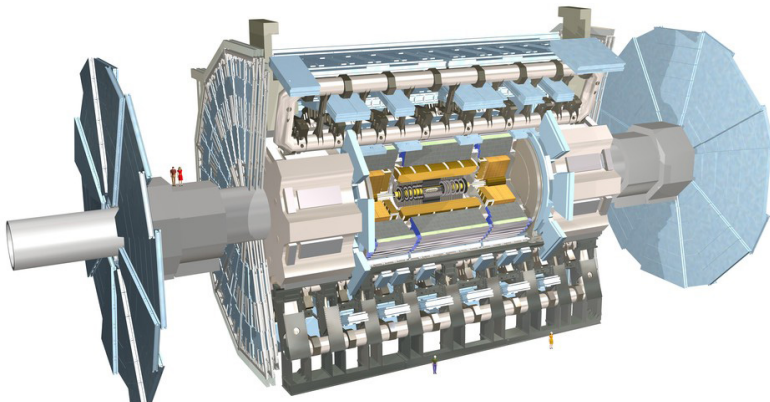


Figure 1.6: ATLAS detector internal view. ©CERN

170 On the human resources side, ATLAS experiment configures a collaboration
171 of around 3000 persons, coming from 117 universities around the world, from 38
172 countries. Thirty percent of the collaboration are students.

173 **LHCb**

174 LHCb detector, hosted at point 8 of the LHC main ring, has a different design than
175 CMS and ATLAS. Smaller than these, its design mainly focus to be able to detect
176 particles produced close to the beam direction. This is the reason why it is not
177 cylindrically but conically shaped, in two detection arms 1.7. It also has the same
178 main parts, a tracking system with a very precise vertex locator, electromagnetic
179 and hadron calorimeters, muon chambers and magnets. Its major specificity is
180 a system that allows to identify different hadrons, the RICH detectors, a crucial
181 feature for the study of strong interacting matter. It measures 21 m long, 10 m
182 high and 13 m wide, and weights 4500 tons. A view of the detector can be found on
183 figure 1.7. The LHCb collaboration groups around 700 persons from 50 different
184 universities over 15 countries.

185 **ALICE**

186 The ALICE experiment (A Large Ion Collider Experiment) is located at point 2
187 of the LHC main ring, measures 16 m high, 16 m wide and 26 m long, and weights
188 10000 tons. Designed for heavy ion physics, it is able to detect an extremely high
189 number of tracks per event. Its main subsystem is the Time Projection Chamber
190 (TPC), a 90 m³ gas chamber filled with a mixture of Ne, CO₂ and N₂ operated in
191 a solenoid of 0.5 T. It allows to measure leptonic and hadronic charged particles in
192 a momentum range from 0.5 to 10 GeV/c. The experiment structure can be seen
193 on figure 1.8. ALICE collaboration counts around 1500 people, from 154 physics
194 institutes in 37 countries.

195 **1.2 The Compact Muon Solenoid (CMS)**
196 **experiment**

197 The CMS detector, hosted at point 5 of the LHC main ring (see figure 1.2), is the
198 second biggest LHC experiment. Cylindrically shaped, measures 15 m of diameter
199 and 28.7 m long, and weights 14000, making it the heaviest LHC experiment. Its
200 subsystems are concentrically located from the collision point in the beam line. It's
201 called compact because the whole calorimetry is inside the solenoid magnet, and
202 muon solenoid because it has a very precise muon detection. Its main characteristic
203 is the strong 3.8 T solenoid magnet. A representation of the detector can be found
204 in figure 1.9. The CMS collaboration is formed by around 2600 scientists, of which
205 900 are students, from 181 institutes over 41 countries.

206 CMS has been designed to be able to do very precise identification of parti-
207 cles originated from the collisions and their properties. For the measurement of

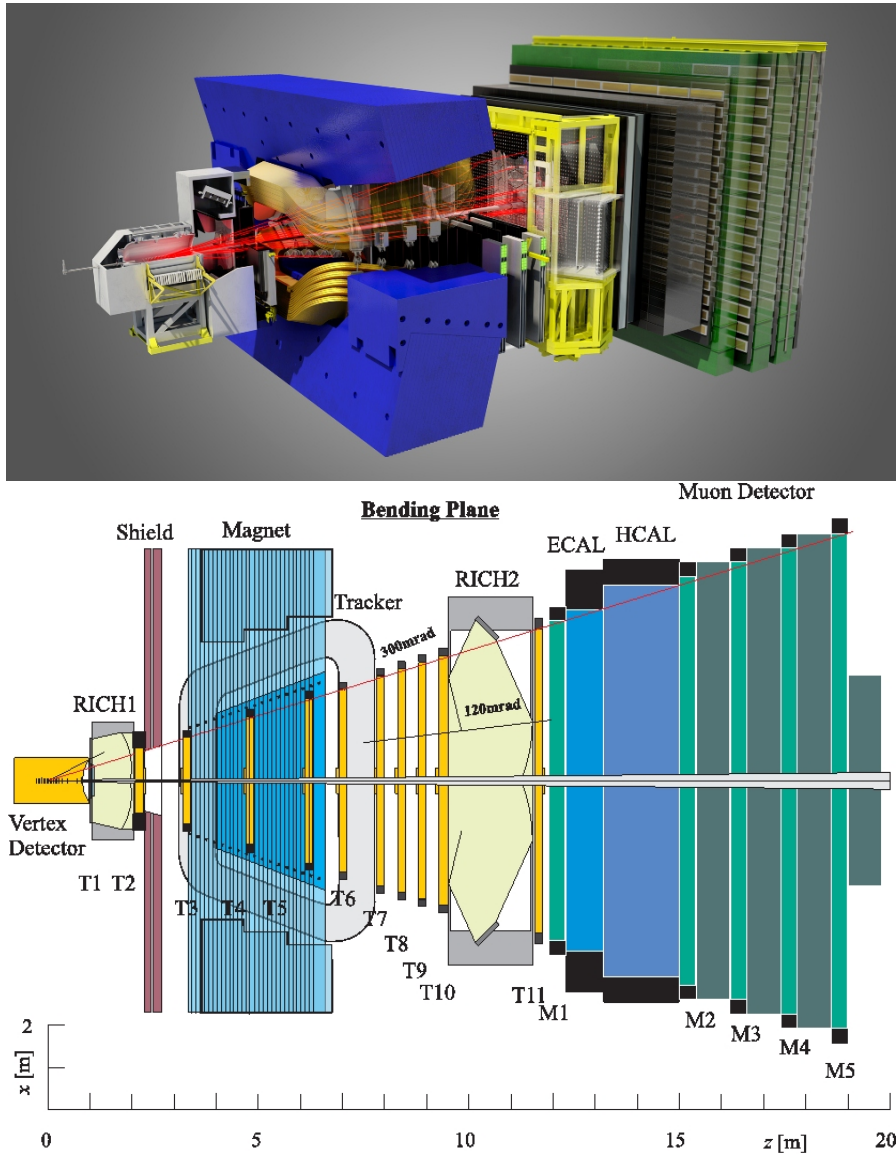


Figure 1.7: LHCb detector internal view [top] and view from the top [bottom].
©CERN

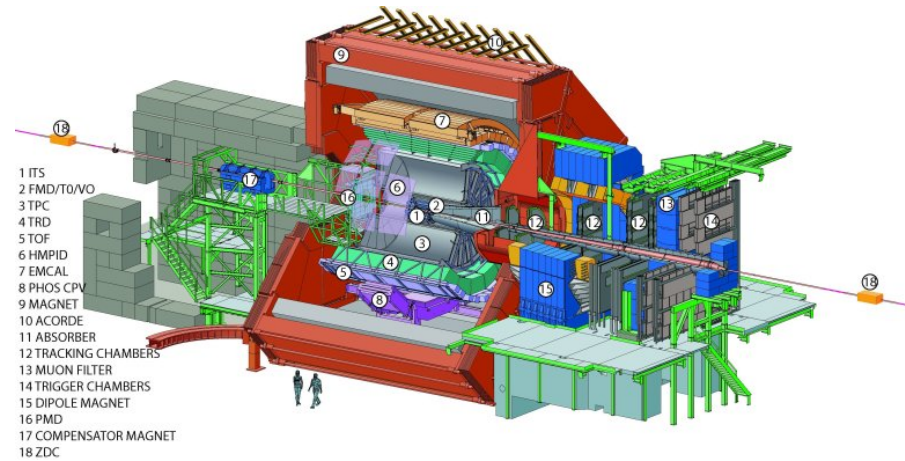


Figure 1.8: ALICE detector internal view. ©CERN

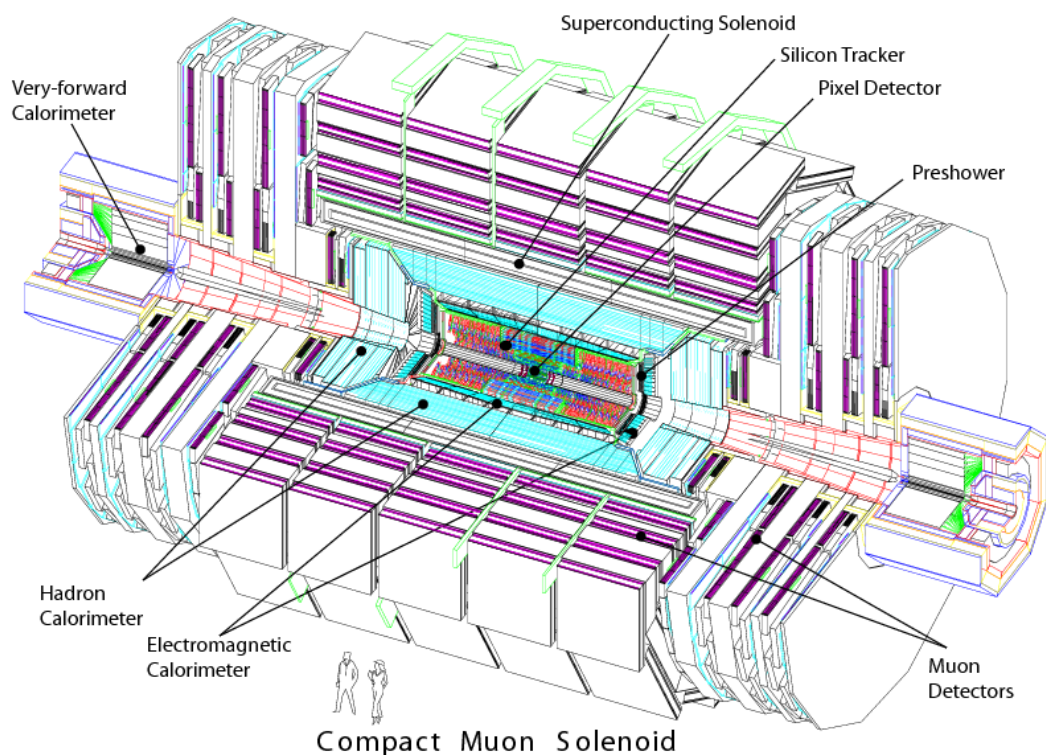


Figure 1.9: CMS detector internal view. ©CERN

the momentum of the charged particles, CMS counts with a very strong magnet that allows to bend very energetic particles. In addition, the calorimeters allow to measure accurately the energy from hadrons, electrons and photons. At the most external layer, the muons chambers measuring muons properties, and in the innermost the tracking system that reconstructs the collision points and the charged particles tracks. In figure 1.10 can be found a representation of the different subsystems of CMS and how particles are reconstructed from them.

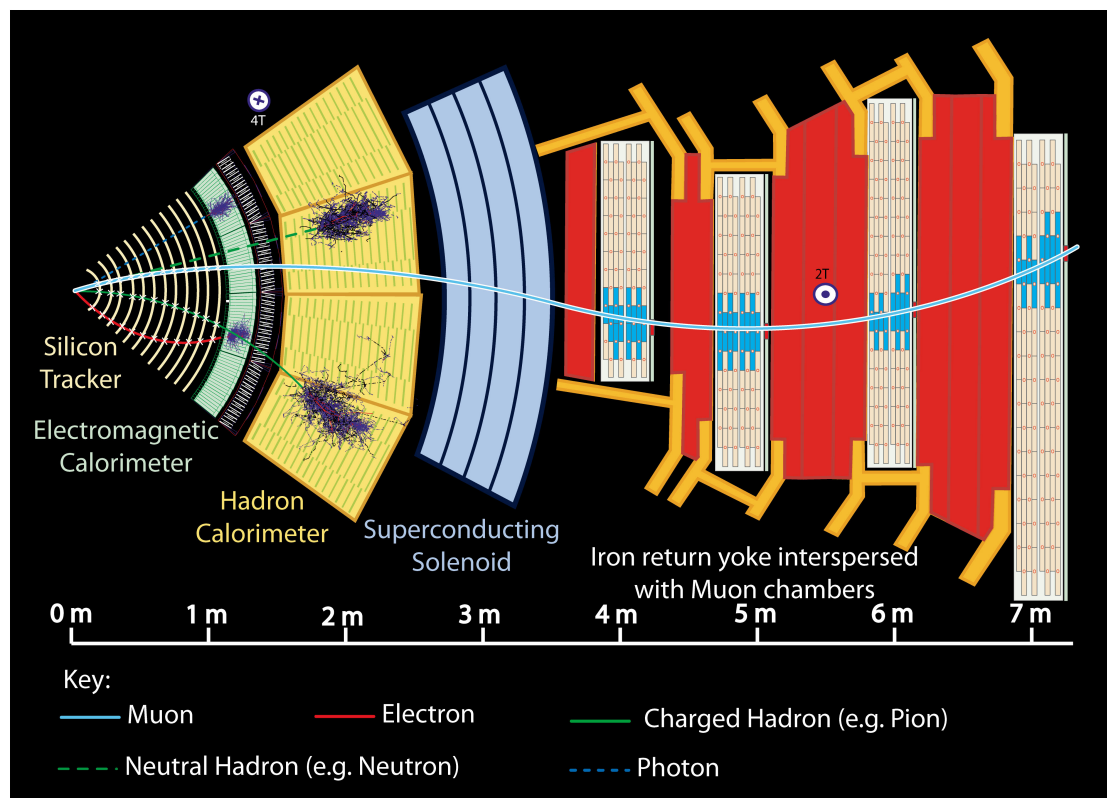


Figure 1.10: CMS sub-detectors and particle identification. ©CERN

1.2.1 Coordinate system

The origin of coordinates defined on the CMS detector is located on the nominal collision point, the “interaction point”. From there, the z-axis is defined along the beam pipe line pointing towards the Jura mountains. The positive/negative z-axis directions define the positive/negative sides of the detector. The y-axis is defined towards the zenith and the x-axis towards the center of the LHC ring. Due to the

221 inclination of the LHC plane, this coordinate system is slightly tilted with respect
 222 to the true vertical. A representation of the coordinate system definition can be
 223 found in figure 1.11.

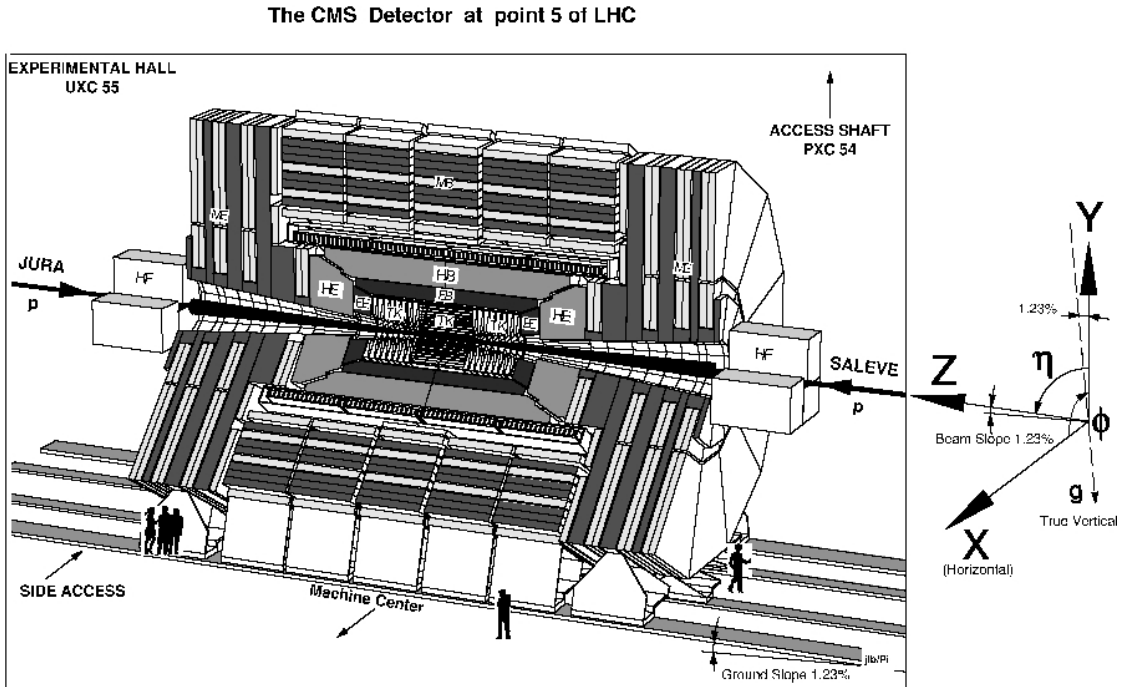


Figure 1.11: CMS coordinate system. ©CERN

224 We can also define two angles: the ϕ angle in the x-y plane from the x-axis
 225 towards the positive y-axis, and the θ angle in the z-y plane from z-axis towards
 226 the positive y-axis. In experimental particle physics is preferred to work with
 227 relativistic invariant quantities, reason why instead of working with θ we define
 228 the pseudorapidity η , equation 1.3.

$$\eta = -\ln \left(\tan \left(\frac{\theta}{2} \right) \right) \quad (1.3)$$

229 One can define another relativistic invariant quantity, the rapidity y as from
 230 equation 1.4. With \mathbf{p} being the momentum vector and E the energy of a given
 231 particle, p_L denotes its longitudinal component, that in our case is the same z-
 232 component.

$$y = \frac{1}{2} \ln \left(\frac{E + p_L}{E - p_L} \right) \quad (1.4)$$

233 On the limit that the mass of the particle is very small compared to its momentum,
 234 one can replace approximate the particle energy by the momentum magnitude,
 235 giving rise to the definition of the pseudorapidity in terms of the momentum of
 236 the particle $\eta = \frac{1}{2} \ln \left(\frac{p+p_L}{p-p_L} \right)$

237 We define also the radial coordinate over the x-y plane, plane that is called
 238 the transverse plane being orthogonal to the longitudinal direction, the z-axis. In
 239 such plane are also defined the transverse quantities of particles, as the transverse
 240 momentum p_T . Finally, for any two objects an angular distance can be defined in
 241 the $\eta - \phi$ plane, as in equation 1.5.

$$\Delta R = \sqrt{(\Delta\eta)^2 + (\Delta\phi)^2} \quad (1.5)$$

242 1.2.2 Magnet

243 In order to measure the momentum of the charged particles going inside the de-
 244 tector is crucial to apply the correct magnet field, sufficiently strong to bend very
 245 energetic particles. The momentum of a charged particle inside an uniform mag-
 246 netic field can be written as

$$p = \gamma mv = qBr \quad (1.6)$$

247 where B is the magnitude of the magnetic field, γ the usual relativistic factor, m
 248 the mass of the particle, v its rapidity, q its charge and r the bending radius. The
 249 sagitta of the arc is

$$s = \frac{L^2}{8r} = \frac{qBL^2}{8p} \quad (1.7)$$

250 with L the trajectory length that the particle moved inside the magnetic field.
 251 Inside a solenoid L is equal to the radius of it.

252 From relation 1.7 it is possible to deduce that the resolution on the momentum
 253 of the particle has an inverse dependence with the magnetic field and the radius
 254 of the solenoid, as shown in equation 1.8. From there, for a better resolution it is
 255 needed to increase the magnetic field and the radius of the solenoid.

$$\frac{dp}{p} \propto \frac{p}{BL^2} \quad (1.8)$$

256 The design of CMS magnet target both features, it utilizes a large solenoid of 6
 257 m of diameter and 13 m long. It's made of 4 layers of windings of NbTi cable that
 258 is cooled to 4.45 K in order to achieve the superconducting state. This magnet is
 259 able to produce an uniform magnetic field inside of it of 3.8 T. Outside the magnet
 260 5 wheels and 3 disks of iron are placed in order to return the flux of the magnetic

261 field, inducing just a 2 T radial magnetic field outside the solenoid. This iron yoke
262 is the main contribution to the detector weight, 10000 tons. The muon chambers
263 are located in between the iron yoke.

264 **1.2.3 Tracker system**

265 The tracker system has been designed to specifically address the reconstruction
266 of high p_T leptons, with particular interest in the isolation of electrons and, as a
267 consequence, to isolate photons. Also the tracker fulfill granularity requirements
268 to reconstruct secondary vertexes to tag and reconstruct B-hadrons. The tracker
269 system is able to reconstruct tracks of particles with at least 2 GeV of p_T with
270 $|\eta| < 2.5$. Charged hadrons are reconstructed with an efficiency of at least 85%
271 for $p_T = 1$ GeV and up to 95% for p_T above 10 GeV. Another important point
272 that was taken into account is the fact that the tracker is the part of CMS most
273 exposed to radiation as it is the closest subsystem to the interaction point. The
274 tracker system was built highly resistant to radiation damage and is expected to
275 last for around 10 years. The pixel detector only lasts 2 years and was replaces
276 during LS1.

277 The tracker has been built with three different technologies: Pixels, Silicon
278 Strips and Micro Strip Gas Chambers (MSGCs). They are arranged concentrically
279 in cylindrical volumes being the pixel detector the innermost and the MSGCs the
280 outermost. The CMS tracker extends to a radius of 155 cm and a around 270 cm
281 on each z direction. The pixel system is in the region with a radius below ≈ 20
282 cm, the silicon detector between ≈ 20 cm and ≈ 60 cm, and the MSGCs between
283 ≈ 70 cm and ≈ 120 cm. The three subsystems are fast enough to work at 25 ns
284 scale.

285 The pixel system is formed by three barrel layers and two end caps disks covering
286 radii from 6 cm to 15 cm. It has an approximate active surface of one square meter
287 with approximately 40×10^6 channels with a cell size of 150 μm by 150 μm . This
288 pixel system allows to obtain three highly precise points that are mainly used for
289 reconstructing vertexes.

290 The Silicon Strip system is formed by a 5-layer barrel (TIB for Tracker Inner
291 Barrel) and 10 disks (TID for Tracker Inner Disks) in each end cap. The strips
292 length is 12.5 cm with a pitch from 61 μm to 122 μm for single-sided strips and for
293 81 μm to 244 μm for double-sided. It's able to achieve a hit resolution of about
294 15 μm .

295 The MSGCs systems is composed of 6 layers in the barrel (TOB for Tracker
296 Outer Barrel) and 11 disks in each end cap (TEC for Tracker EndCap, with a \pm
297 sign depending on the z direction). Here the strips are 10 cm length for the inner
298 layers and 25 cm for outer layers with a pitch from 200 μm to 400 μm , which gives a
299 hit resolution of 35 μm and 100 μm respectively. The MSGCs and Silicon systems

300 have an overall active area of around 300 m^2 with 12×10^6 channels organized in
 301 more than ten thousand independent modules.

302 In figure 1.12 can be seen the disposition of all the tracker subsystems. From the
 303 design of the tracker system the best resolution on the p_T measurement is achieved
 304 in the $|\eta| < 1.6$ region, this due to the presence of more layers of detector in the
 305 different subsystems, as shown in figure 1.13.

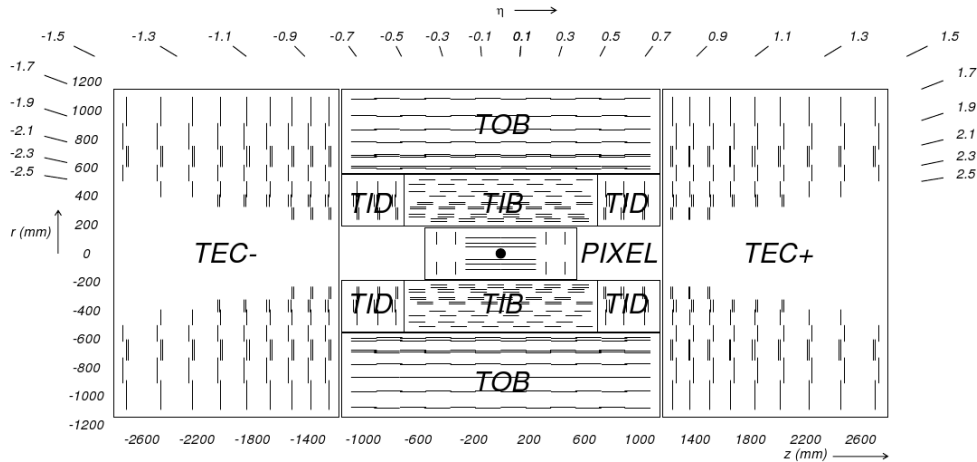


Figure 1.12: CMS tracker system configuration. ©CERN

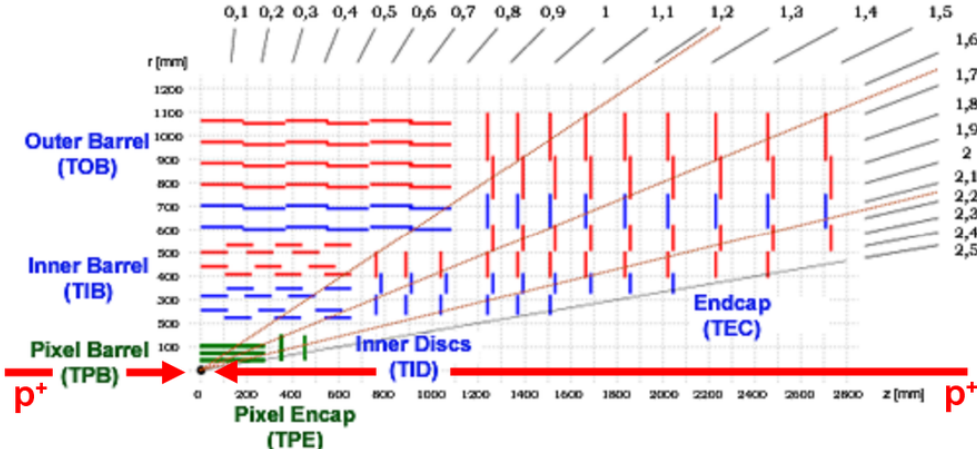


Figure 1.13: Tracker resolution with η . ©CERN

306 ■

Two plots: on pixel resolution and

307 efficiency on finding hits ■

308 **1.2.4 Electromagnetic calorimeter**

309 The CMS ECAL (Electromagnetic CALorimeter) is the detector subsystem de-
310 signed to stop photons and electrons to measure their energy. It's an hermetic
311 cylindrical calorimeter made of 61200 crystals in the barrel ($|\eta| < 1.479$) and 7324
312 in each end cap ($1.48 < |\eta| < 3$). The crystals material is lead-tungstate that
313 is transparent, very dense (8.28 g/cm^3), has a small Moliere radius (2.2 cm) and
314 a short radiation depth ($X_0 = 0.89 \text{ cm}$). This material has been chosen for the
315 characteristics already described, but also because is very fast emitting the scin-
316 tillation light (in 25 ns), it has a very good energy resolution and resistance to
317 radiation. The crystals are distributed in 36 super-modules, 1700 crystals each, in the
318 the barrel (EB for ECAL Barrel) and in four 'Dee's, of 3662 crystals each, in the
319 end caps (EE for ECAL End cap). In the EB the scintillation light is collected
320 by Avalanche Photo-Diodes, or APD, and by Vacuum Photo-Triodes, or VPT, in
321 the EE. A preshower system is installed in face of each end cap to allow a better
322 discrimination between photons and π^0 's. A representation of the CMS ECAL can
323 be found on figure 1.14.

324 ■ Plot on cristal response, dielec-
325 tron reconstruction on the ECAL, ratio of
326 E/p for reconstructed electrons E from the
327 ECAL and p from the tracker ■

328 **1.2.5 Hadronic Calorimeter**

329 The CMS HCAL, for Hadronic CALorimeter, is the subdetector designed to mea-
330 sure the energy of hadrons produced in the collisions, mainly the neutral hadrons
331 because the charged hadrons are already traced by the tracker. It's also designed
332 to measure the missing energy coming from particles not being detected by any
333 of the subsystems, as neutrinos. It's an hermetic set of subsystems covering up to
334 $|\eta| < 5.2$:

- 335 • Hadron Barrel Calorimeter (HB): Covering $|\eta| < 1.4$ is located between the
336 ECAL barrel and the magnet.
- 337 • Hadron Endcap Calorimeter (HE): Extends the coverage of the barrel on the
338 region $1.4 < |\eta| < 3$.

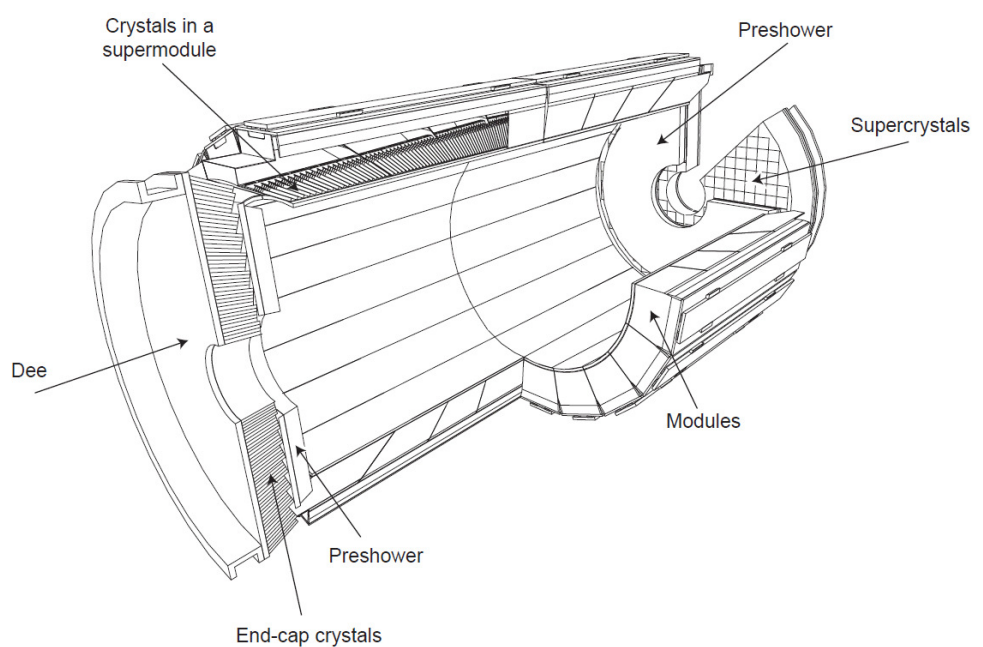


Figure 1.14: CMS ECAL representation. ©CERN

- 339 • Hadron Outer Calorimeter (HO): Located outside the magnet, uses it as an
 340 additional absorber.
- 341 • Hadron Forward Calorimeter (HF): Completes the coverage of the system
 342 from $|\eta| = 3$ up to $|\eta| = 5.2$.

343 The CMS HCAL layout is shown in figure 1.15. The system is made of two
 344 parts, an absorber to develop the hadronic showers and a scintillator to measure
 345 the particles energy. The length scale of hadronic calorimetry is designated as the
 346 interaction length corresponding to the mean free path of an hadron in a material.
 347 The HB absorber is made of 40 mm thick steel plate, eight layers of brass plates of
 348 50.5 mm thick, six brass plates of 56.5 mm thick and a steel plate of 75 mm thick.
 349 The HE uses the same absorber but with thicker plates, of 79 mm. Between the
 350 absorber plates a plastic scintillator, Kuraray SCSN81, of 3.7 mm thick is placed.
 351 In the region with $|\eta| < 1.6$ the achieved granularity is $\Delta\eta \times \Delta\phi = 0.087 \times 0.087$
 352 and $\Delta\eta \times \Delta\phi = 0.17 \times 0.17$ in the region with $|\eta| > 1.6$. This design gives a total
 353 of 70000 tiles used. The produced light in the HB is collected by optical fibers and
 354 transferred to the Hybrid Photo Diodes (HPDs). This diodes were chosen thanks
 355 to their small sensitivity to the magnetic field, an important feature due to the
 356 proximity of the HCAL to the magnet.



Figure 1.15: CMS HCAL representation. ©CERN

357 The HF design is very different from the rest of the HCAL subsystems. The
 358 most important challenge for the HF is the high resistance to radiation, while in

359 the central rapidity region 100 GeV are deposited in average in the forward region
360 is 760 GeV. For this reason it was chosen a Cherenkov detector made of quartz
361 fibers with a steel absorber. The light produced in the HF is collected by photo
362 multipliers.

363 **1.2.6 Muon chambers**

364 The muon system of CMS is located at the most exterior layer of the detector due to
365 the penetration power of this particle. Muons are not stopped by the calorimeters
366 and, with neutrinos, they are able to escape the detector. The muon chambers
367 are placed in a cylinder around the HO and in disks on the end caps. Three main
368 characteristics have been fulfilled from the design: efficient muon identification,
369 precision measurement of muon charge and momentum and fast measurement
370 to provide trigger capabilities. The moun chambers are made of three different
371 subsystems:

- 372 • Drift Tubes Chambers (DT): Located in the region with $|\eta| < 1.2$ and dis-
373 posed in four layers. They consist of individual drift tubes of $50 \mu\text{m}$ of
374 diameter anode wire with two electrode plates creating a drift electric field.
375 The wall of the cell act as cathode. The cells are filled with a gas mixture,
376 85% Argon and 15% CO_2 . The tubes are organized in plaques that are also
377 organized in SuperLayers (SL) each one made of 4 plaques. The barrel is
378 made of 250 DT's disposed in four cylinders separated by iron yokes.
- 379 • Cathode Strip Chambers (CSC): Installed in the end caps, provide a coverage
380 up to $|\eta| = 2.4$ from $|\eta| = 0.9$. These chambers are multi-wire proportional
381 chambers made of six planes of anode wires with 7 cathode planes. Four
382 CSC stations are placed in each end cap. The wires are oriented in azimuthal
383 direction while the cathode planes are radially oriented, allowing a complete
384 measurement of the position of the particle. This system is able to measure
385 with a precision between the $75 \mu\text{m}$ and $150 \mu\text{m}$.
- 386 • Resistive Plate Chambers (RPC): This subsystem is made of gaseous parallel
387 plate detectors. This detector is specially useful for triggering as it is very
388 fast and have a good position resolution. There are 480 RPC distributed in
389 6 layers in the barrel with the DT and in 3 layers in the end caps with the
390 CSC, and covers the region with $|\eta| < 1.6$.

391 On figure 1.16 can be found a representation of the muon system with the
392 different components. The DT and CSC system cover $|\eta| < 2.4$ without any gap.

393  Plot of
394 RPC efficiency during Run1 and L1 RPC

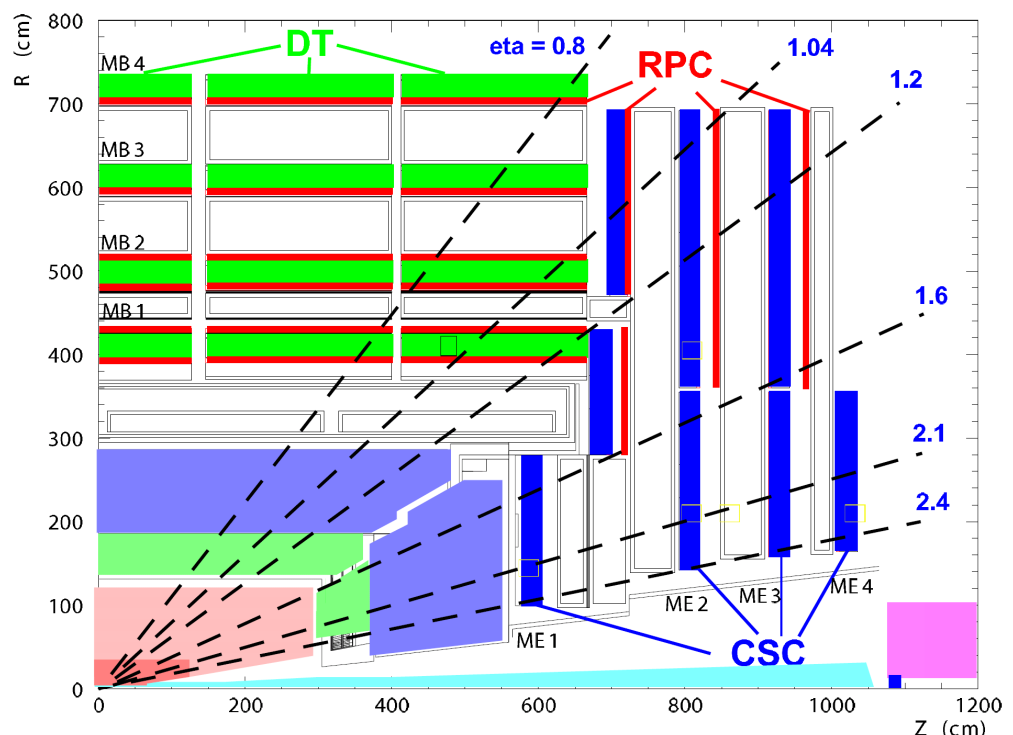


Figure 1.16: CMS muon chambers representation. ©CERN

395 efficiency as function of probe PT ■

396 **1.2.7 Trigger**

397 LHC has been designed to provide experiments with proton-proton collisions every
398 25 ns, meaning a frequency of 40 MHz. Each recorded event by CMS has a nominal
399 size between 0.5 and 1 MB, what means a data flux of around $10^9 \text{ MB/s} = 1\text{PB/s}$
400 that is extremely big for transfer and for storing. Therefore, an on-line selection
401 of events has to be done. The trigger system of CMS does this task in two fold,
402 a level 1 (L1) and a high level trigger (HLT). The L1 is hardware based and the
403 HLT is software based.

404 From the searches conducted at CMS, the interesting events produced on proton-
405 proton collisions for new physics searches are very rare. The enormous majority of
406 events coming from proton-proton collisions correspond to well understood phe-
407 nomena, while new physics events are 'exotic' with regards to the most common
408 type of events. Then is interesting to keep only a part of the events, what actually
409 eases the analysis afterward done over the data.

410 The CMS trigger system is designed to keep only 100 kHz tops by the L1 and
411 300 Hz by the HLT. L1 is reducing the data flux by 2 orders of magnitude and the
412 HLT another 3 orders of magnitude.

413 **Level 1 trigger**

414 The L1 is designed to trigger over coarse data coming from the calorimeters and
415 muon chambers, holding data in pipe-lined memories in the front-end electronics.
416 Therefore, relies on very fast reconstruction of objects coming from this subsys-
417 tems: muons, electrons, photons, jets and missing energy. This reconstruction
418 differs from the final reconstruction of the objects, for example a jet for the L1
419 consists on successive energy deposits in the ECAL and HCAL, while the off-line
420 reconstruction take into account also the tracker information.

421 The L1 starts from regional data coming from the subsystems which is after-
422 ward combined in order to build ranked trigger objects in localized regions of the
423 detector. Global Muon and Calorimeter triggers sort the objects and send the best
424 ranked to the Global Trigger (GT). Before the GT no events are rejected, is only
425 with the GT that the selection is applied. The GT combines the information and
426 can apply topological requirements and take a decision on keeping or disregarding
427 the event. On figure 1.17 can be found the work-flow of the L1.

428 The L1 cards are distributed between the detector and an adjoin cavern at 90
429 m distance from the detector. The latency time L1 disposes between the collision
430 and the taking of the decision is about $3.2 \mu\text{s}$. Therefore, the front-end memory
431 in the cards should be able to keep in memory up to 128 bunch crossings.

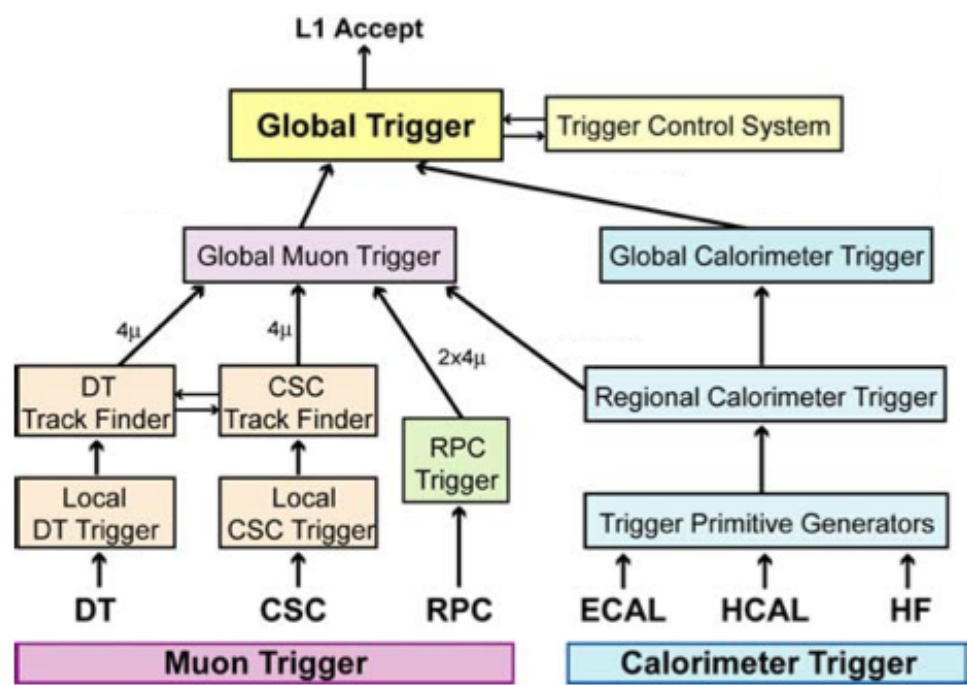


Figure 1.17: L1 architecture. ©CERN

432 **High Level Trigger**

433 The HLT take as input the events accepted by the L1 and process them using farms
434 of commercial processors. The HLT does additional operations on the selected
435 events making it much slower than L1 processing. In particular, the HLT takes also
436 into account the tracker information. Consequently, this system is able to take into
437 consideration the whole information of the detector. However, the reconstruction
438 of objects done by the HLT differs slightly from the final off-line reconstruction.
439 The decision taking process takes around 40 ms, 10^4 times more than for L1.

440 The events selected by HLT are finally stocked on disks under several paths
441 depending on the selection performed. There is a constant development of HLT
442 paths focusing on different analysis requirements in order to obtain the best pos-
443 sible selection efficiency for specific signal types.

444 **1.3 Object reconstruction**

445 **1.3.1 Track and vertex reconstruction**

446 ■ Plots: Tracker efficiency
447 reconstruction for muons and single pions
448 as function of pt and eta ■

449 **Vertex reconstruction**

450 ■ Two plots: Primary vertex resolutions
451 and Primary vertex efficiency ■

452 **1.3.2 Particle Flow (PF) algorithm**

453 **Calorimeter clustering**

454 **Subdetectors link**

455 ■ Two plots: Link of tracks to ECAL and
456 to HCAL ■

457 **Particle reconstruction**

458 **1.3.3 Electron reconstruction**

459 ■ Plot of electron efficiency. Table with
460 electron ID requirements ■

461 **1.3.4 Muon reconstruction**

462 ■ Plots: PF muon efficiency selection,
463 dimuon mass spectra ■

464 **1.3.5 Jet reconstruction**

465 **Clustering algorithms**

466 **SISCone**

467 **kT**

468 **Cambridge-Aachen**

469 **Anti-kT**

470 **Infrared and collinear safety**

471 **Jet area** ■ Plots: Jet in y-phi-pT space for
472 each algorithm ■

473 **Jet energy corrections**

474 ■ Plot of JEC uncertainty as pT function
475 and eta ■

476 **b-jets identification**

477 **Identification algorithms and working points** ■ Plots:
478 CSV discriminator, Nb of secondary ver-
479 tices, Efficiency of b-tagging for CSVM as
480 function of PT and eta ■

⁴⁸¹ 2 The Standard Model

⁴⁸² Since the Greeks, different theories about the composition and structure of the
⁴⁸³ world have been formulated. At ancient Greece these theories were elaborated
⁴⁸⁴ from a philosophical point of view. Nowadays, we count with a very sophisticated
⁴⁸⁵ set of tools and concepts that allowed us to build up a general vision of nature,
⁴⁸⁶ its components and structure. Moreover, on the subject of the constituents, or
⁴⁸⁷ elemental constituents, a theory capable of describing the majority of known phe-
⁴⁸⁸ nomena has been developed. This theory is the Standard Model (SM) of particle
⁴⁸⁹ physics.

⁴⁹⁰ This SM relies in two of the more elegant constructs of modern physics and
⁴⁹¹ mathematics. From the physics side, the quantum field theory; from mathematics,
⁴⁹² group theory. Quantum field theory has born from the understanding of processes
⁴⁹³ that take place at very small spatial scales and in a regime where special relativity
⁴⁹⁴ play an important role. To describe such, a major part of the most brilliant minds
⁴⁹⁵ of the 20th century dedicated their life, Paul Dirac, Richard Feynman, Enrico
⁴⁹⁶ Fermi among them. The theory of quantum fields has set in a common place two
⁴⁹⁷ extraordinary achievements of physics: special relativity and quantum mechanics.
⁴⁹⁸ With it we have been capable to describe many phenomena: β and α decay, solid
⁴⁹⁹ state, among many other.

⁵⁰⁰ From the mathematics side, group theory has become one of the most powerful
⁵⁰¹ tools for particle physicist. However, their development began quite early, with
⁵⁰² Galois around 1830, and was used in other parts of physics, it's with Lie algebras
⁵⁰³ and the possibility of describing continuous symmetries that the most important
⁵⁰⁴ step were given. Also, this would have not been possible with the amazing connec-
⁵⁰⁵ tion found by Emmy Noether in 1918. She found that for every conserved quantity
⁵⁰⁶ there is a preserved symmetry. Group theory can be seen, roughly speaking, a way
⁵⁰⁷ to mathematically describe symmetries, group theory became the tool to describe
⁵⁰⁸ systems with conserved quantities.

⁵⁰⁹ In this chapter, we present the basics of the SM. We describe its seminal ideas,
⁵¹⁰ its structure and content and its ultimate consequences. Finally, we close with its
⁵¹¹ limitations.

512 2.1 Fields, symmetries and interactions

513 From the very beginning of physics, one of the most fundamental questions has
 514 been how does bodies interact, and what is exactly an interaction. On the first
 515 type of interaction ever studied by physics, gravity, Newton proposed the con-
 516 cept of distant interaction, the idea that bodies could interact without being in
 517 direct contact. But the question on how exactly that distant action was performed
 518 remained unanswered.

519 During the 19th and 20th century new phenomena were discovered pointing to
 520 brand new interactions, electricity, magnetism and radioactivity. The very precise
 521 and complete description of electromagnetism developed by Gauss, Faraday, Am-
 522 père and finished by Maxwell arrived to describe electricity and magnetism under
 523 the formalism of only one interaction within the mathematical formalism of classi-
 524 cal fields. Further works addressed radioactivity, driving to a deeper understanding
 525 of nature and its composition.

526 For the following discussion, and later, we are going to work in natural units
 527 for simplicity. In these units the speed of light c is normalized to unity, as well as
 528 electron electric charge e , reduced Planck constant \hbar and Boltzmann constant k_B .
 529 Then, masses and temperature are expressed in energy units, i.e. eV , and time
 530 and length in inverse energy units, eV^{-1} .

531 A classical field is an assignment of a quantity to every point in space and time.
 532 For physics, the quantity that is attributed is a physical quantity such as mass,
 533 electrical charge or probability. This quantity can be scalar or vector, giving rise to
 534 the notion of scalar or vector field, correspondingly. The simplest example, is the
 535 temperature in a gas, that is a scalar quantity assigned to every point. Another
 536 example, a fluid can be described in terms of fields, being the velocity of the fluid
 537 a vector field and its pressure a scalar field. Generic classical electromagnetic
 538 interactions can be described with the help of one vector field $\vec{A}(x)$, the vector
 539 potential, and one scalar field $\phi(x)$, the scalar potential. In the formalism of
 540 four-vectors from relativistic dynamics one can organize these two quantities in the
 541 four-potential $A_\mu = (-\phi, \vec{A})$. This can be used to define the strength field tensor
 542 $F_{\mu\nu} = \partial_\mu A_\nu - \partial_\nu A_\mu$, where $\partial_\mu = \left(-\frac{\partial}{\partial t}, \nabla\right)$ is the covariant derivative. From the
 543 tensor it is possible to obtain in a very generic and elegant way the equations of
 544 motion of the free field using the Lagrangian formalism, as in equation 2.1. With
 545 the Lagrangian density defined in equation 2.2.

$$\partial_\mu \left(\frac{\partial \mathcal{L}}{\partial(\partial_\mu A_\nu)} \right) - \frac{\partial \mathcal{L}}{\partial A_\nu} = 0 \quad (2.1)$$

$$\mathcal{L} = -\frac{1}{4} F^{\mu\nu} F_{\mu\nu} \quad (2.2)$$

546 It's very important to notice that the equations of motion of the free field are
 547 invariant under the choice of the four-potential. More precisely, the covariant
 548 potential is not unique and we can always add the covariant derivative of a scalar
 549 field,

$$A'_\mu = A_\mu + \partial_\mu \Lambda(x) \leftrightarrow \partial^\mu A_\mu = 0 \quad (2.3)$$

550 and describe the same physics. This non-uniqueness corresponds to the choice
 551 of a zero-point of the potential very well known in non-Lagrangian formalism of
 552 electrodynamics. When we choose a specific value for this scalar field, $\Lambda(x)$, we
 553 say that the gauge has been fixed.

554 One can also define a four current vector, $J_\mu = (\rho, \vec{J})$ with ρ the electric charge
 555 density and \vec{J} the current charge density. Then, plugging in this four current in
 556 the Lagrangian of the free field, defined in equation 2.2,

$$\mathcal{L} = -\frac{1}{4} F^{\mu\nu} F_{\mu\nu} - A_\mu J^\mu \quad (2.4)$$

557 we can obtain the complete set of equations of motion of the field with charges
 558 and currents.

559 The transformation stated from equation 2.3 can be understood as a transfor-
 560 mation of the field. These type of transformations are mathematically understood
 561 under the group $U(1)$, where the generic transformation operator can be written
 562 as $U = e^{i\theta(x)}$. It's said then that the electromagnetic vector potential is *invariant*
 563 under $U(1)$ transformations. This property identifies an essential characteristic of
 564 electromagnetism, its symmetric behavior under $U(1)$.

565 From this reasoning the most interesting results are drawn when the same sym-
 566 metry is imposed to another fields. For example, the kinetic Lagrangian for a
 567 complex scalar field is $\mathcal{L} = (\partial^\mu \phi)^* \partial_\mu \phi$. To perform the transformation on the
 568 scalar field, it is sufficient to apply the operator as $\phi' = U\phi$ and $\phi'^* = \phi^* U^{-1}$. But
 569 it's evident that the Lagrangian is not the same after applying such transforma-
 570 tion. Then, in order to preserve the Lagrangian under $U(1)$ is necessary to change
 571 at the same time the derivative. Such transformation is given in equation 2.5,
 572 where g is a constant.

$$\mathcal{D}^\mu = \partial^\mu - ig A^\mu \quad (2.5)$$

573 Then, the proposed Lagrangian can be rewritten, including the vector field, as

$$\mathcal{L} = (\mathcal{D}^\mu \phi)^* \mathcal{D}_\mu \phi - \frac{1}{4} F^{\mu\nu} F_{\mu\nu} \quad (2.6)$$

574 that is invariant under $U(1)$. An interaction term, of the form $ig A^\mu \phi^* \partial_\mu$, between
 575 the scalar and the vector field, can be derived from the kinematic part of the
 576 Lagrangian $\mathcal{D}^\mu \phi)^* \mathcal{D}_\mu \phi$. This shows that the requirement of the invariance under

577 $U(1)$ of the scalar field lead to the introduction of an interaction with a vector field
578 controlled by the constant g . We have also seen that electromagnetic interaction
579 is described precisely by a vector field and that preserves $U(1)$ symmetry, which
580 implies that this symmetry is the connection to electromagnetic interaction, iden-
581 tifying the interaction itself with the $U(1)$ symmetry. In addition, using Noether
582 theorem one can show that g is a conserved quantity, as the electric charge is.

583 But not only electromagnetism can be described via a continuous symmetry as
584 $U(1)$. On 1896 radioactivity was discovered by the french physicist Henri Bec-
585 querel. Three years after, Marie and Pierre Curie studied in more detail the
586 phenomenon and found Polonium and Radium elements. And later on, Ernst
587 Rutherford was able to describe radioactivity as coming in three types, alpha (α),
588 beta (β) and gamma (γ). He also noticed that radioactivity was able to change
589 matter, which allowed him, with also other experiences, to propose an atomic
590 model, describing elements as basically and external core of negative charges and
591 a nucleus positively charged. Consequently, This findings implied the existence of
592 interactions different to electromagnetism, acting at the atomic scale.

593 The interaction that undergoes radioactivity, beta decay, is called the weak
594 interaction. In 1933 Enrico Fermi made a first theoretical description of this in-
595 teraction, but only in 1968 Sheldon Glashow, Abdus Salam and Steven Weinberg
596 were able to describe weak interaction with a symmetry group: $SU(2)$. Finally,
597 the interaction that keeps the nucleus components together, the strong interaction,
598 was described with $SU(3)$ group mainly by Murray Gell-Mann in 1963.

599 There have been many attempts to describe gravity with the same formalism,
600 but up to present such attempts have been unsuccessful. Such question remains
601 one of the most important problems for modern particle physics.

602 **2.2 Quantum fields and particles**

603 Classical fields, introduced and described in last section 2.1, can be extended to a
604 quantum theory. Such procedure is known as the quantization of fields and allow
605 to unify special relativity and quantum mechanics in one theory, Quantum Field
606 Theory (QFT), to describe the dynamics of systems in such regimes: speed close
607 to the speed of light on the atomic or smaller scales.

608 Quantum mechanics introduced two fundamental concepts: first, the description
609 of the system by its states; and second, the identification of an observable with
610 an operator. The state of a system is identified with a set of quantum numbers
611 that tell us the characteristics of the system when is at some state. For example,
612 the hydrogen atom system has energy as quantum number, such that each state
613 has a value for the energy describing the potential energy contained in the system.
614 Quantum states are mathematically noted in Dirac notation as a *ket*,

$$|\alpha\rangle = |i, j, k, \dots\rangle \quad (2.7)$$

with α the set of quantum numbers i, j, k, \dots . This mathematical object lives in Hilbert space (a complex space \mathbb{C} of functions), which conjugate, a *bra*, is noted $\langle\alpha|$, and their internal product $\langle\beta|\alpha\rangle$. The numerical value of $|\langle\beta|\alpha\rangle|^2$ gives the transition probability of the system from state β to state α , and $|\langle\alpha|\alpha\rangle|^2$ is the probability to find the system in state the α .

Physical observables as position, energy or momentum are described by complex operators such that to measure their value for a given state, one just have to calculate $|\langle\alpha|\hat{O}|\alpha\rangle|^2$. The identification of observables and operators is called *first quantization*. In addition, Schrodinger equation describes the evolution of states,

$$\hat{\mathcal{H}}|\alpha\rangle = i\frac{d}{dt}|\alpha\rangle \quad (2.8)$$

with \mathcal{H} the Hamiltonian of the system. The whole formalism is able to explain *quantized* systems, where the quantum numbers are discrete, such as hydrogen atom or black body.

Several functions or fields can be related to a given state. These functions, wave functions, can be used as the states to calculate probabilities. In *second quantization* wave functions are upgraded into field operators. This procedure gives rise to the quantization of the state of the field, which is described by the quantum number n which is definite positive. $n = 0$ for the fundamental state and $n > 0$ for the excited states. Such excitations of the field are understood as physical particles that propagates in space-time, which means that $n = 0$ is vacuum.

The first QFT ever created was born from the quantization of the electromagnetic field. Quantum Electro Dynamics (QED) is the quantized version of classical electrodynamics, that was developed by Tomonaga, Schwinger and Feynman around 1960. This theory describes electromagnetic interactions of a charged field and the electromagnetic vector field. The charged field excitations correspond to electrons and the excitations of the vector fields are photons, responsible of light. Electrons are a particle with negative electric charge and orbit around the nucleus in atoms. Discovered in 1897 by J. J. Thomson, it was fully described by P. A. Dirac in 1928 with the Dirac equation that is the Schrodinger equation for a relativistic particle of spin $1/2$. Spin, the intrinsic angular momentum carried by a particle, can be integer $(0, 1, 2, \dots)$ or semi-integer $(\frac{1}{2}, \frac{3}{2}, \dots)$. The particles with semi-integer spin, as electrons, are called *fermions* and particles with integer spin, as photons, are called *bosons*. Dirac equation predicted the existence of a particle identical to the electron but with positive charge, the positron. It was discovered on 1932 by Carl David Anderson.

Up to present days we have found 12 fundamental fermions and 5 fundamental bosons. Fermions are organized in *leptons*, that don't interact strongly, and *quarks*, that do interact strongly. Leptons are as well organized in three families, the electron (e^-) and electron neutrino (ν_e), muon (μ^-) and muon neutrino (ν_μ) and tau (τ) and tau neutrino (ν_τ). Electron, muon and tau are electrically charged while neutrinos are neutral. Their respective anti-particles are equally organized, positron (e^+) with electron anti-neutrino ($\bar{\nu}_e$), anti-muon (μ^+) with muon anti-neutrino ($\bar{\nu}_\mu$) and anti-tau (τ^+) with tau anti-neutrino ($\bar{\nu}_\tau$). Quarks also come in three families, with the respective anti-quarks: up (u, \bar{u}) and down (d, \bar{d}), charm (c, \bar{c}) and strange (s, \bar{s}), top (t, \bar{t}) and bottom (b, \bar{b}). The fundamental bosons are the photon (A), the W (positively and negatively charged) and Z that mediate the electroweak interaction, the gluon (g) mediating the strong interaction and the Higgs (H). The weak bosons were discovered at CERN in 1983 at the UA1 and UA2 collaborations over the SPS accelerator (described on section 1.1.1). The Higgs boson has been discovered recently on 2012 by ATLAS and CMS experiments at the LHC. The 2013 physics Nobel prize was awarded to Francois Englert and Peter W. Higgs "for the theoretical discovery of a mechanism that contributes to our understanding of the origin of mass of subatomic particles, and which recently was confirmed through the discovery of the predicted fundamental particle, by the ATLAS and CMS experiments at CERN's Large Hadron Collider".

2.2.1 The mass problem

Using the concepts developed on later sections about QFT and symmetries it's possible to construct a whole theory giving rise to a precise description of particles and interactions between them. But such a theory does not allow to have massive bosons, whereas masses for fermions are allowed. A mass term for a fermion ψ is of the form

$$m_\psi \bar{\psi} \psi$$

where m_ψ is the mass of the field.

Under $U(1)$ transformations, $\psi' = U\psi$, the mass term remains the same, what means that is invariant under $U(1)$ transformations. The same is not true for a boson. A mass term for a boson A , can be written as

$$m_A A^\mu A_\mu \quad (2.9)$$

where m_A is its mass.

The $U(1)$ transformation for the boson is $A'^\mu = A^\mu + \delta^\mu \theta(x)$. Applying such transformation on the mass term 2.10 one can obtain the transformed term

$$m_A (A^\mu A_\mu + A^\mu \delta_\mu \theta(x) + \delta^\mu \theta(x) A_\mu + \delta^\mu \theta(x) \delta_\mu \theta(x)) \quad (2.10)$$

683 where the last three terms make this term not invariant under $U(1)$ transformations.
 684 Consequently, one can say that a mass term for the boson destroy the
 685 invariance of the theory under $U(1)$ symmetry.

686 Nonetheless there is no need for a theory of a massive photon, there is a need to
 687 have massive bosons for weak interactions. There is a relation between the mass of
 688 a boson and the range of the interaction mediated by it. Massless bosons transmit
 689 long range interactions, as electromagnetism, but short range interactions, as the
 690 weak interaction, are mediated by massive bosons. More precisely the interaction
 691 range is inversely proportional to the mass of the boson, higher the mass shortest
 692 the range. Such relation can be seen from the structure of the propagator, which
 693 is a mathematical entity that describes the probability a particle has to travel
 694 a distance in a given time. Such propagator, for a vector boson, has a generic
 695 form given in equation 2.11, where k_μ is the momentum carried by the boson. It's
 696 clear from this structure that a massive boson has less probability to travel a long
 697 distance than a massless boson in a given time.

$$\frac{g_{\mu\nu}}{k^2 - m^2 + i\epsilon} \quad (2.11)$$

698 Then, as massive bosons are requires for weak interaction, somehow the $SU(2)$
 699 symmetry has to be broken. There are basically two ways to broke a symmetry:

- 700 • Explicit symmetry breaking: By the introduction of a symmetry breaking
 701 term in the Lagrangian, as a mass term for the bosons.
- 702 • Spontaneous symmetry breaking: When the ground state of one field fail to
 703 be invariant under the symmetry.

704 Explicit symmetry breaking is not an option, because the symmetry needs to be
 705 preserved in the Lagrangian in order to introduce the interaction.

706 2.2.2 Spontaneous Symmetry Breaking

707 Several physical systems exhibit an spontaneous symmetry breaking. For example,
 708 a pencil balanced on its tip is perfectly symmetric system around the vertical axis,
 709 however, because of the instability of the system the pencil will eventually fall
 710 over. The final state is stable but not symmetrical. This transition also decreased
 711 the potential energy of the system, driving the system to its ground state. This
 712 means that whereas the system had a symmetry the ground state does not show
 713 the symmetry. In general, symmetry breaking is linked to phase transitions, as
 714 liquid to gas transition or magnetization of a ferromagnet, covering a plethora of

715 physical processes. To a greater extent, in recent studies, [8], the emergence of life
 716 has been understood as a phase transition of matter.

717 To achieve an spontaneous symmetry breaking of $SU(2)$ in QFT one should
 718 choose a field for which its ground state, vacuum, will fail the symmetry. This
 719 means, in practical terms, that such field will have a non-zero value in vacuum,
 720 leading to a presence of particles coming from the field on theory vacua. If a
 721 fermion field is chosen, the vacuum will show a preference on directionality de-
 722 pending on its spin orientation, what breaks Poincaré symmetry imposed by spe-
 723 cial relativity. The same is true if a spin-1 bosonic field is chosen for the task. In
 724 order to avoid this problem a spin-0 field should be used. In addition, this field
 725 should be electrically neutral to avoid having a charged vacuum.

726 Whit all this properties in mind, taking a scalar doublet of $SU(2)$, defined on
 727 equation 2.12 where ϕ^0 and ϕ^+ are complex fields, the most general potential can
 728 be written from two auto-interaction terms, in equation 2.13.

$$\Phi = \begin{pmatrix} \phi^+ \\ \phi^0 \end{pmatrix} = \begin{pmatrix} \phi^+ \\ \phi_{RE} - i\phi_{IM} \end{pmatrix} \quad (2.12)$$

$$V(\Phi) = \mu^2 \Phi^\dagger \Phi + \lambda (\Phi^\dagger \Phi)^2 \quad (2.13)$$

729 Such potential has a unique minimum for $\lambda > 0$ and $\mu^2 > 0$, but for $\lambda > 0$ and
 730 $\mu^2 < 0$ has a set of minima with the shape of “Mexican hat”, shown in figure 2.1.
 731 Under $\lambda > 0$, $\mu^2 < 0$ configuration the field breaks spontaneously the symmetry
 732 reaching the ground state, acquiring an expectation value on vacuum different
 733 from zero, v .

734 2.2.3 Englert-Brout-Higgs mechanism

735 After the spontaneous symmetry breaking, the scalar doublet transforms into the
 736 form given in equation 2.14, where G^+ and G^0 are the Goldstone bosons product
 737 of the breaking of the $SU(2)$ symmetry, and H is the Englert-Brout-Higgs boson.
 738 From Goldstone’s theorem when a symmetry is spontaneously broken a massless
 739 boson appear for each broken generator. In our specific case, the three generators
 740 of $SU(2)$ are broken giving rise to three Goldstone bosons: G^+ , G^- and G^0 . This
 741 massless bosons are “eaten” by the W^+ , W^- and Z^0 giving them an additional
 742 degree of freedom, the longitudinal polarization.

$$\Phi = \begin{pmatrix} G^+ \\ \frac{1}{\sqrt{2}}(H + v - iG^0) \end{pmatrix} \quad (2.14)$$

743 By this mechanism, the W and Z bosons acquire mass, being its value set by the
 744 coupling constant of $SU(2)$ group and the vacuum expectation value of Englert-

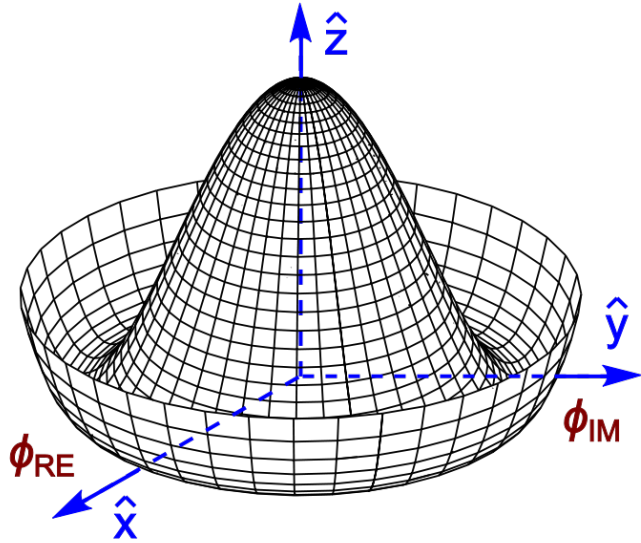


Figure 2.1: Higgs potential

⁷⁴⁵ Brout-Higgs boson. In addition, the fermions on the theory also acquire a mass
⁷⁴⁶ from the interactions with the scalar doublet. Such masses are in general of the
⁷⁴⁷ form $m_f = \lambda_f v / \sqrt{2}$, where λ_f sets the interaction between the Englert-Brout-
⁷⁴⁸ Higgs boson and the fermion. Finally, also the Englert-Brout-Higgs boson has a
⁷⁴⁹ mass $m_H^2 = -2\mu^2$.

⁷⁵⁰ In summary, with this mechanism the weak interaction bosons and fermions of
⁷⁵¹ the theory are given a mass on the price of introducing an additional scalar field
⁷⁵² to spontaneously break the $SU(2)$ symmetry.

⁷⁵³ 2.3 Top production at LHC

⁷⁵⁴ 2.3.1 Pair production

⁷⁵⁵ ■ ⁷⁵⁶ Plots of cross
⁷⁵⁷ section of ttbar production as function of
⁷⁵⁸ center of mass energy; Feynman diagrams
 for pair production ■

759 **2.3.2 Single t production**

760 ■ Plots of cross sec-
761 tion of single-top production as function of
762 center of mass energy; Feynman diagrams
763 for single production ■

764 **2.3.3 Decay channels**

765 ■ Plot
766 on possible decay channels and branching
767 ratios to each channel; Feynman diagram
768 for each decay channel ■

769 **2.3.4 Top properties**

770 **Electric charge**

771 **Lifetime**

772 **Mass and width**

773 ■ Plot of top mass measurement from
774 Tevatron+LHC combination ■

775 **Spin correlation**

776 **2.4 Higgs production at LHC**

777 ■ Plots of cross
778 section of Higgs production as function of
779 center of mass energy; Feynman diagrams
780 for Higgs production ■

781 **2.4.1 Decay channels**

782 ■ Plot
783 on possible decay channels and branching
784 ratios to each channel; Feynman diagram
785 for each golden bb and diphoton channels
786 ■

787 **2.4.2 Higgs properties**

788 **Electric charge**

789 **Spin**

790 ■ Plot on spin-parity measurement of
791 Higgs boson ■

792 **Mass and width**

793 ■ Plot on ATLAS+CMS combination
794 of the Higgs mass; Plot on signal strength
795 for each decay channel; Individual plots on
796 diphoton channel and golden channel ■

797 **2.5 Hierarchy problem and other limitations**

798 The SM has been one of the most successful theories on the history of physics.
799 With only 19 free parameters, is able to make thousands of predictions that have
800 been measured and tested over the last seventy to eighty years. However some
801 aspects in the model are not completely understood. The most important one
802 is the so-called hierarchy mass problem. At tree level, the Englert-Brout-Higgs
803 boson has a mass $m_H^2 = -2\mu^2$, but the physical mass also contain the one-loop
804 contributions from fermions that interact with it, as the top quark. The Feynman
805 diagram for such contribution can be seen in figure 2.2.

806 Such contributions add up giving a mass greater than simple tree level mass.
807 Each fermion contributes proportionally to its mass, what means that the top
808 quark contributes the most. Moreover, if there are in nature heavier fermions that

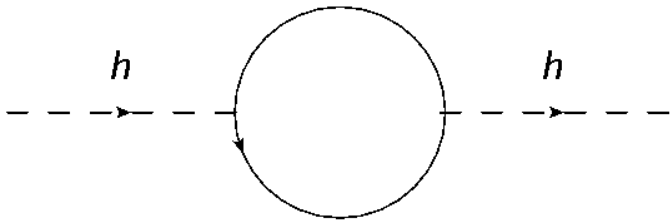


Figure 2.2: One loop diagram for contributions to the mass of the Englert-Brout-Higgs boson from interactions with fermions

also interact with the Englert-Brout-Higgs boson they will also contribute to its mass. With such considerations one can expect the Englert-Brout-Higgs boson to be much greater than 125 GeV, and in principle not even of the order of 100 GeV but greater than 1 TeV. However the real relevance or significance of this problem at theoretical level has been discussed extensively, for example at [9], the majority of the community agrees there is something to be understood on the subject.

The most famous proposed solution to this problem is supersymmetry (SUSY) [10]. It proposes the existence of an additional symmetry between fermions and bosons, at a given point of the history of universe nature didn't distinguish between fermions and bosons. However, we know this does not happen at the present, and then this symmetry should be broken. Such symmetry implies the existence of a super-symmetric partner for each particle, a super-partner. A fermion for each boson and vice versa. This SUSY procedure doubles the particle content of the model where it's applied. Before breaking SUSY, a particle and it's partner have the same mass. In this feature is where the hierarchy problem is solved. On figure 2.3 one can see the one loop diagrams for the mass of the Englert-Brout-Higgs boson from the top and its super-partner the stop. Whereas, the top contribution is positive, the stop contribution is negative but equal in value, then cancelling between them.

But this solution works exactly only if SUSY is not broken. As we know SUSY has to be broken, there has been developed in the literature different ways to break SUSY and still offer a solution to the hierarchy problem, leading normally to solutions that need a fine adjustment of the parameters of the theory. This represents for some theoreticians a problem itself: Fine-tuning or Naturalness. Extensive searches for SUSY particles have been performed, accordingly to different model realizations MSSM [11, 12], CMSSM, etc.

While hierarchy problem is an internal problem of the SM, there are several questions that have not been solved. For example, how gravity is understood in the frame of QFT's, why there is only 3 generations of leptons and quarks, why there is only 4 fundamental forces among others. In addition, there have

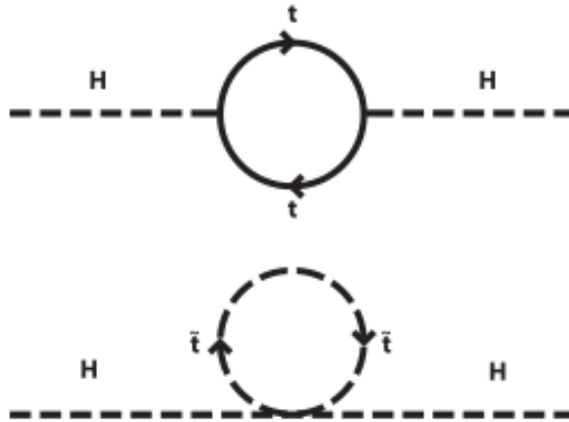


Figure 2.3: One loop diagrams for contributions to the mass of the Englert-Brout-Higgs boson from the top and the stop

839 been experimental questionings to the SM. The mos important one is the masses
 840 of neutrinos. In the SM neutrinos are massless, careful measurements, [13, 14],
 841 have shown that neutrinos can oscillate between different flavors, phenomenon
 842 only possible if neutrinos have a mass. Measurements of solar and atmospheric
 843 neutrino oscillations have been the most important proof of physics beyond the
 844 SM.

845 From cosmological measurements, the Wilkinson Microwave Anisotropy Probe
 846 have shown that the universe is not only made by visible matter, but suggests that
 847 around 24% its made of dark matter. A type of matter not visible by means of
 848 light. It has also shown that 71% of the universe is composed of dark energy, what
 849 makes the universe to be in an accelerated state of expansion. These results can
 850 be seen in [15, 16]. Also the Planck probe has shown similar results, for example
 851 in [17]. The SM does not have any answer to this open problems so far.

852 Finally, there is known that the universe presents an asymmetry between mat-
 853 ter and antimatter, being the first much more abundant than the second. Such
 854 asymmetry can be obtained by CP-violating processes (C for charge and P for
 855 parity). However the amount of CP violation present in the SM is not compatible
 856 with the huge matter-antimatter asymmetry in nature. This problem, known as
 857 baryon asymmetry, represent an additional huge challenge for particle physics.

858 In conclusion, the SM has been a formidable model that has helped us to under-
 859 stand a huge amount of physics. It has done thousands of predictions that have
 860 been measured and corroborated one by one in the last half-century. However,

861 this is not the end of the story, perhaps only the beginning. There are theoretical
862 and experimental motivations that lead us think that the SM is not the “final”
863 theory that could explain all subatomic phenomena in nature. Currently, there is
864 a mayor effort, both theoretical and experimentally, to understand and explain all
865 the remaining pieces. The present work is one of them.

866 In the next chapter, we present an extension of the SM that looks for a solution
867 to the discussed hierarchy problem.

868 **3 Vector Like Quarks: Generic 869 model**

870 From chapter 2 we have seen how there are some parts in the SM that does
871 not work very well. From such internal issues some further models/theories have
872 been developed. All this theories are commonly grouped under the term Beyond
873 Standard Model or simply BSM. One of the most famous BSM theory is super-
874 symmetry (SUSY). This theory postulates a symmetry that does not distinguish
875 between fermions and bosons. This idea have given birth to a plethora of model
876 realizations and physics predictions. So far, nothing of the new consequences of
877 this theory have been confirmed but the experiments have an enormous invest-
878 ment on their search. But not only SUSY have seen the day light, there is on the
879 market an astonishing amount of BSM theories addressing different issues of the
880 SM. Extra dimensions, fourth families, composite Higgs are a few of them.

881 In this chapter we will describe a bunch of models that introduce additional
882 heavy quarks, heavier than the top, in order to solve the hierarchy problem, de-
883 scribed on section 2.5.

884 **3.1 Motivation**

885 **3.2 Generic Formulation**

886 ■ Table with different possible
887 representations and assigned charges ■

888 **3.2.1 Production modes**

889 ■ Plot of pro-
890 duction cross section at LHC for different
891 energies as function fo the mass. Feynamn
892 diagrams of the production processes. ■

893 **3.2.2 Decay modes**

894 ■ Plot
895 of branching ratio as function of the mass
896 for different scenarios (representations) ■

897 **3.3 Fesability study for a search of a T at LHC at 8
898 TeV**

899 **3.3.1 Stragey for the full hadronic final state**

900 ■ Table
901 with cross sections and expected events for
902 each bakcground process and signal. Plot
903 of eta of jet produced with T ■

904 **3.3.2 Event selection**

905 ■ $N - 1$ plots for selection variables.
906 Efficiency table. ■

907 **3.3.3 Results**

908 ■ Expected yields table. Final M5J plot. ■

909 4 Understanding theory predictions 910 via Monte-Carlo event generation

911 Although we have nowadays a very elegant and complete theoretical description
912 of particle physics, is not always evident how to translate this theory in actual
913 predictions, to compare with measurements. Moreover, on the case of hadronic
914 colliders, as the LHC, it's even more difficult due to the particularities of strong
915 interaction. On this subject, a set of tools and approaches have been developed in
916 order to be able to make accurate predictions from theory that could be directly
917 researched for on the experiments, as CMS or ATLAS for example. In the present
918 chapter, we describe such tools and formalisms and a set of studies comparing the
919 predictions these tools to data.

920 4.1 Mote-Carlo simulations

921 The Monte-Carlo simulations use random numbers and large samplings to calcu-
922 late mathematical quantities in complex configurations, as integrals or probabili-
923 ties. The typical example is on how to calculate the integral of a one-dimensional
924 function. One can throw several random coordinates pair in the Cartesian plane
925 and count how many of them are under the function. Then the integral of the
926 function will be proportional to the fraction of points under the curve to the total
927 thrown points. Larger the number of points, closer the estimation to the real value.
928 An illustration of the procedure can be seen in figure 4.1.

929 A similar method is used to simulate proton-proton collisions. This simulation is
930 used to generate “random” events and to calculate quantities, as the cross section,
931 for a given physical process. Each event represent the final state of a collision, i.e.
932 the set of particles produced from the collision and seen by a detector. Such simu-
933 lations comprehend different stages: first, the partonic processes making reference
934 to the interaction between the partons inside the proton; second, the hadroniza-
935 tion of the particles produce from parton interactions; and third, the simulation of
936 the interaction between the hadrons (from second step) and the detector material.
937 Such events are used to evaluate predictions from theory in the frame of a specific
938 experiment. Whereas the hadronization and detector simulation are well-known
939 physical processes, new theories predictions rely basically on the partonic level,

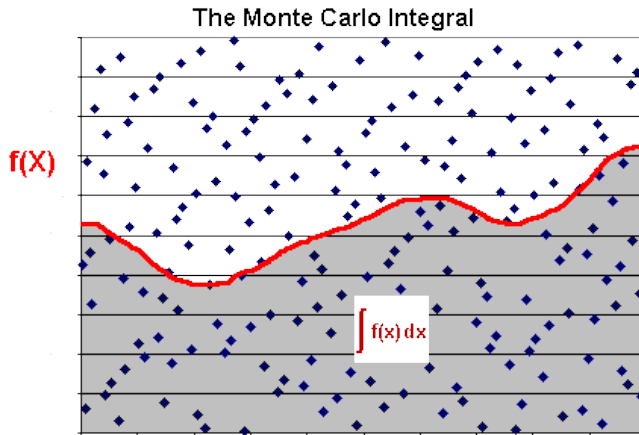


Figure 4.1: Integration using Monte-Carlo methods

940 where the fundamental interaction processes take part.

941 **4.1.1 Parton simulation**

942 The parton model was initially proposed by Richard Feynman in 1969, as a method
 943 to understand collisions of non-fundamental particles. The model consider a non-
 944 fundamental particle, as a proton or a neutron, composed of a given number of
 945 point-like fundamental particles. When a collision occur the point-like particles
 946 inside have a major probability to scatter. For example, when an electron is fired
 947 against a proton the most of the interactions will between the electron and the
 948 fundamental components of the proton, u and d quarks. This “hard” components
 949 are called *valence* quarks. Surrounding them there are the *sea* quarks and gluons.

950 However, as the energy of the collision increases the probability to scatter a sea
 951 component, quark or gluon, increases. In addition, even if the valence quarks of a
 952 proton are the u and d quarks, heavier quarks can appear in the sea, as the b , c or s
 953 quarks. The probability to interact with a component, valence or sea, is described
 954 by parton distribution function, commonly called PDF. A PDF $f \equiv f(x, Q^2)$ rep-
 955 resent the number density of a given quark or gluon as a function of the energy
 956 scale Q^2 and the fraction of momentum carried by the parton x . The determina-
 957 tion of a PDF is done via a fit of large data samples from experiments specifically
 958 designed to test the inner structure of nucleons. The DIS (Deep Inelastic Scat-
 959 tering) experiment at SLAC (Stanford Linear Accelerator Center), in California,
 960 United States, first probed the existence of partonic structure inside nucleons us-
 961 ing leptons as probes scattered against nucleons. Another important experiment
 962 was the HERA accelerator at DESY in Hamburg, Germany, which used electrons

963 to study the inner structure of protons.

964 In figure 4.2 is shown the Martin-Stirling-Thorne-Watt [18] (MSTW) PDF for
 965 two energy scales. The MSTW PDF is one of the experimental fits combining data
 966 from DIS and HERA. In this PDF can be seen that u and d quarks carry the most
 967 of the momentum of the proton. The rest of the momentum is spread mainly over
 968 a huge amount of gluons and some, less probable, sea quarks as \bar{u}, \bar{d} or c and s .
 969 One important feature is that the composition of the proton changes depending
 970 on the energy scale. At $Q^2 = 10 \text{ GeV}^2$ there is no b -quark in the proton while at
 971 $Q^2 = 10^4 \text{ GeV}^2$ there is a non-negligible probability to find it in the proton.

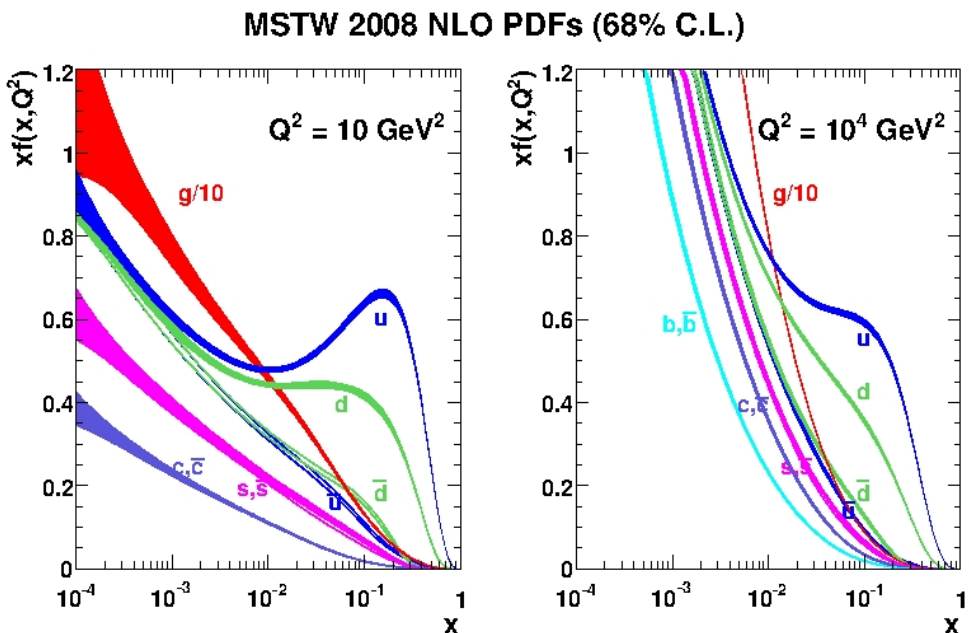


Figure 4.2: Martin-Stirling-Thorne-Watt proton PDF for $Q^2 = 10 \text{ GeV}^2$ [left] and $Q^2 = 10^4 \text{ GeV}^2$ [right]. From [18]

972 Two other important PDF fits are CTEQ [19] and NNPDF [20]. Together with
 973 MSTW, they are the most used PDF sets in the CMS experiment for MC produc-
 974 tion.

975 For the hard process, the differential cross section can be written as,

$$\begin{aligned}
d\sigma_{ij \rightarrow lm} &= \left(\int_0^1 \int_0^1 f_i(x_i, Q^2) f_j(x_j, Q^2) dx_i dx_j \right) \\
&\times \frac{d^3 p_l}{(2\pi)^2 2E_l} \frac{d^3 p_m}{(2\pi)^2 2E_m} \delta^4(p_i + p_j - p_l - p_m) \\
&\times |\mathcal{M}_{ij \rightarrow lm}|^2
\end{aligned} \tag{4.1}$$

where $f_{i,j}$ correspond to the PDF's of the initial partons. $\mathcal{M}_{ij \rightarrow lm}$ is the matrix element of the process which is the part of the S-matrix that contains the amplitude of the process, and modules the transition from the initial to the final state [21]. The matrix element could account effectively for all processes mediating the transition from the initial to the given final state, but in practice it is calculated only including a given number of processes. The calculation can achieve different levels, usually tree level or Leading Order (LO), but modern calculation could arrive, depending on the process, to one loop or Next-to-Leading-Order (NLO) or even two loops the Next-to-Next-to-Leading-Order (NNLO). This limit depends exclusively on the feasibility of the theoretical calculations. In figure 4.3 is shown an example of a leading order plus its corresponding NLO diagrams for a fermion scattering.

4.1.2 Hadron simulation

■ Figure to illustrate to hadronization process ■

4.1.3 Detector simulation

4.2 Tools

4.2.1 Matrix-element generators

4.2.2 Hadron generators

4.3 Validation on data

■ Plot of W+jets and Z+jets comparison between data and MC for a set of different generators. Plot on top pt to briefly introduce tpo pt reweighting ■

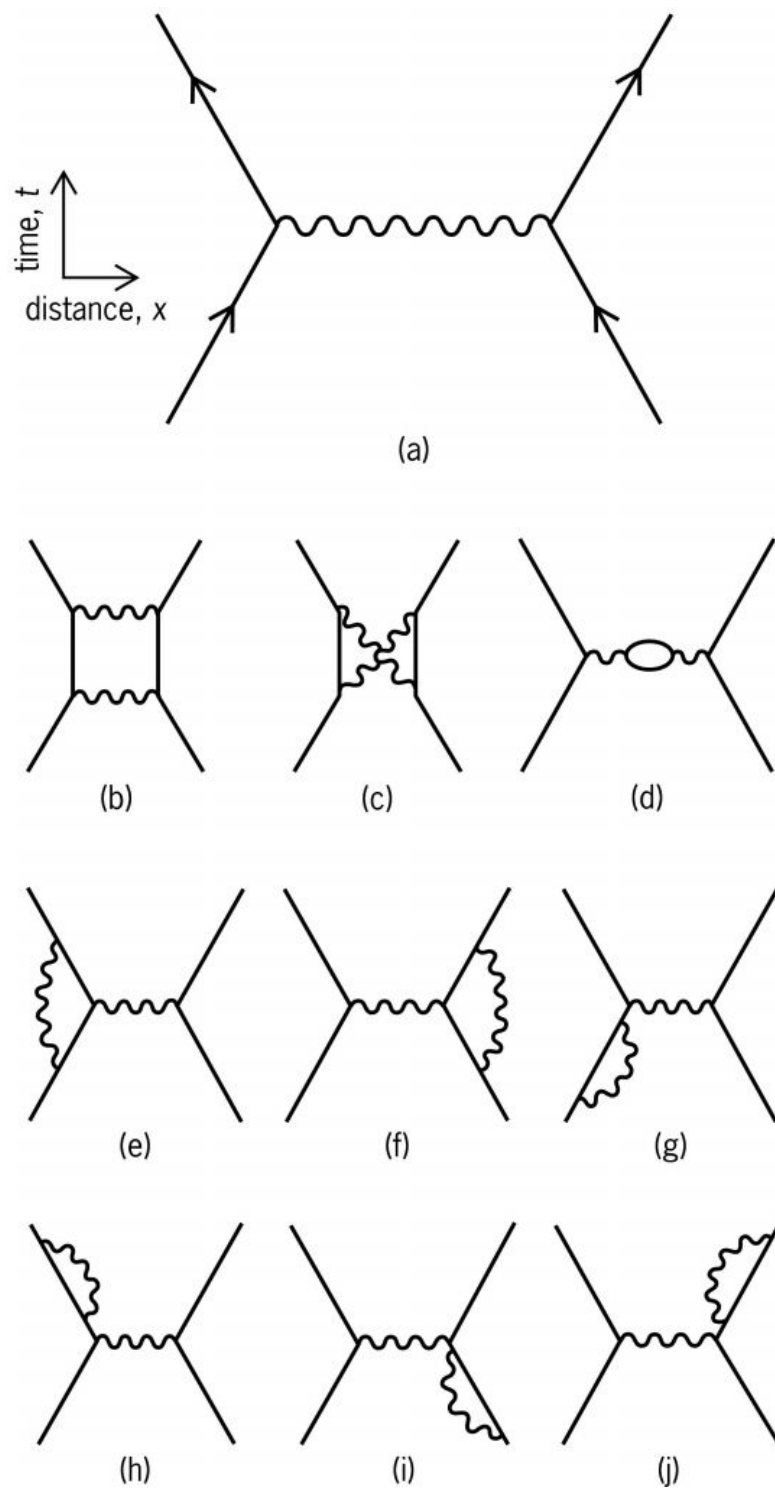


Figure 4.3: LO (a) and NLO (b)-(j) processes contributing to fermions scattering

999 **5 Search for a single produced T'**
1000 **decaying into top and Higgs in**
1001 **the full hadronic final state**

1002 In the present chapter we describe in full detail the search performed using 2012
1003 data collected by CMS for a T' in the full hadronic final state. The theoretical
1004 formalism for such object has been described on chapter 3.

1005 **5.1 Analysis Strategy**

1006 **5.2 Datasets**

1007 ■ Table with Multijet primary
1008 datasets and integrated luminosity. Tables
1009 for MC samples, backgrounds and signal
1010 mass points. ■

1011 **5.3 Event selection**

1012 **5.3.1 Event processing**

1013 **5.3.2 Basic selection**

1014 ■ Plots of pt and eta
1015 of six leading jets, number of vertices, HT
1016 and number of CSV b-tagged jets ■

1017 **5.3.3 T' reconstruction with a χ^2 sorting algorithm**

1018 ■ Table with inclusive and exclusive
1019 reconstruction efficiency. Plots of mass of
1020 reconstructed T, W, H and top right after
1021 reconstruction for all mass points. Table
1022 with gaussian fit results. ■

1023 **5.3.4 Selection based on reconstructed objects**

1024 ■ $N - 1$ plots for object selection variables.
1025 Table with S/B and $S/\sqrt{S + B}$ from MC
1026 for each step of the selection. ■

1027 **5.3.5 Efficiencies**

1028 **Trigger**

1029 ■ Trigger efficiency plots ■

1030 **Selection**

1031 ■ Table with efficiencies of full
1032 selection. Plot with selection efficiency for
1033 all mass points. ■

1034 **5.4 Background estimation from data**

1035 **5.4.1 Known difficulties and tried methods**

1036 ■ 2D plot of $pT(H)$
1037 and $pT(\text{top})$ to show correlation and ta-
1038 ble with ttbar+QCD and signal content in

₁₀₃₉ each region from ABCD method based on
₁₀₄₀ $pT(H)$ and $pT(\text{top})$ ■

₁₀₄₁ **5.4.2 Method**

₁₀₄₂ **5.4.3 Validation**

₁₀₄₃ ■ Validation plots: MC, Data. Chi2
₁₀₄₄ plots for minimization. Number of com-
₁₀₄₅ binations in the control sample plot. Plot
₁₀₄₆ of M_{5J} for different values of chi2. Ta-
₁₀₄₇ ble with signal contamination percentage
₁₀₄₈ in the control sample cut per cut and for
₁₀₄₉ all mass points. ■

₁₀₅₀ **5.5 Systematics**

₁₀₅₁ ■ Tables for PDF, b-tagging and JEC
₁₀₅₂ systematics. Table with full systematics. ■

₁₀₅₃ **5.6 Results**

₁₀₅₄ ■ Expected and observed yields table.
₁₀₅₅ Exclusion limits plot. M_{5J} plot for data
₁₀₅₆ with estimated background and signal. ■

1057

Bibliography

- 1058 [1] O. S. Brüning, P. Collier, P. Lebrun, S. Myers, R. Ostoja, J. Poole, and
1059 P. Proudlock, *LHC Design Report*. CERN, Geneva, 2004.
- 1060 [2] **CMS Collaboration** Collaboration, G. L. Bayatian *et al.*, *CMS Physics:*
1061 *Technical Design Report Volume 1: Detector Performance and Software*.
1062 Technical Design Report CMS. CERN, Geneva, 2006. There is an error on
1063 cover due to a technical problem for some items.
- 1064 [3] **CMS Collaboration** Collaboration, G. L. Bayatian *et al.*, “CMS Physics:
1065 Technical Design Report Volume 2: Physics Performance,” *J. Phys. G* **34**
1066 no. CERN-LHCC-2006-021. CMS-TDR-8-2, (2007) 995–1579. 669 p. revised
1067 version submitted on 2006-09-22 17:44:47.
- 1068 [4] **ATLAS Collaboration** Collaboration, A. Collaboration, *ATLAS detector
1069 and physics performance: Technical Design Report*. Technical Design Report
1070 ATLAS. CERN, Geneva, 1999. Electronic version not available.
- 1071 [5] **LHCb Collaboration** Collaboration, J. Alves, A. Augusto *et al.*, “The
1072 LHCb Detector at the LHC,” *JINST* **3** (2008) S08005.
- 1073 [6] **ALICE Collaboration** Collaboration, P. Cortese, C. W. Fabjan,
1074 L. Riccati, K. Safarík, and H. de Groot, *ALICE physics performance:
1075 Technical Design Report*. Technical Design Report ALICE. CERN, Geneva,
1076 2005. revised version submitted on 2006-05-29 15:15:40.
- 1077 [7] **UA4/2 Collaboration** Collaboration, C. Augier *et al.*, “Predictions on the
1078 total cross-section and real part at LHC and SSC,” *Phys.Lett.* **B315** (1993)
1079 503–506.
- 1080 [8] C. Mathis, T. Bhattacharya, and S. Imari Walker, “The Emergence of Life
1081 as a First Order Phase Transition,” *ArXiv e-prints* (Mar., 2015) ,
1082 arXiv:1503.02776 [nlin.AO].
- 1083 [9] F. Jegerlehner, “The hierarchy problem of the electroweak Standard Model
1084 revisited,” arXiv:1305.6652 [hep-ph].

- 1085 [10] S. P. Martin, “A Supersymmetry primer,” *Adv.Ser.Direct.High Energy Phys.*
 1086 **21** (2010) 1–153, [arXiv:hep-ph/9709356 \[hep-ph\]](#).
- 1087 [11] **CMS** Collaboration, V. Khachatryan *et al.*, “Search for neutral MSSM
 1088 Higgs bosons decaying to a pair of tau leptons in pp collisions,” *JHEP* **1410**
 1089 (2014) 160, [arXiv:1408.3316 \[hep-ex\]](#).
- 1090 [12] **ATLAS** Collaboration, G. Aad *et al.*, “Search for neutral Higgs bosons of
 1091 the minimal supersymmetric standard model in pp collisions at $\sqrt{s} = 8$ TeV
 1092 with the ATLAS detector,” *JHEP* **1411** (2014) 056, [arXiv:1409.6064 \[hep-ex\]](#).
- 1093 [13] **Super-Kamiokande** Collaboration, Y. Ashie *et al.*, “Evidence for an
 1094 oscillatory signature in atmospheric neutrino oscillation,” *Phys.Rev.Lett.* **93**
 1095 (2004) 101801, [arXiv:hep-ex/0404034 \[hep-ex\]](#).
- 1096 [14] C. Weinheimer and K. Zuber, “Neutrino Masses,” *Annalen Phys.* **525**
 1097 no. 8-9, (2013) 565–575, [arXiv:1307.3518](#).
- 1098 [15] C. L. Bennett, D. Larson, J. L. Weiland, N. Jarosik, G. Hinshaw,
 1099 N. Odegard, K. M. Smith, R. S. Hill, B. Gold, M. Halpern, E. Komatsu,
 1100 M. R. Nolta, L. Page, D. N. Spergel, E. Wollack, J. Dunkley, A. Kogut,
 1101 M. Limon, S. S. Meyer, G. S. Tucker, and E. L. Wright, “Nine-year
 1102 Wilkinson Microwave Anisotropy Probe (WMAP) Observations: Final Maps
 1103 and Results,” *The Astrophysical Journal, Supplement* **208** (Oct., 2013) 20,
 1104 [arXiv:1212.5225 \[astro-ph.CO\]](#).
- 1105 [16] G. Hinshaw, D. Larson, E. Komatsu, D. N. Spergel, C. L. Bennett,
 1106 J. Dunkley, M. R. Nolta, M. Halpern, R. S. Hill, N. Odegard, L. Page,
 1107 K. M. Smith, J. L. Weiland, B. Gold, N. Jarosik, A. Kogut, M. Limon, S. S.
 1108 Meyer, G. S. Tucker, E. Wollack, and E. L. Wright, “Nine-year Wilkinson
 1109 Microwave Anisotropy Probe (WMAP) Observations: Cosmological
 1110 Parameter Results,” *The Astrophysical Journal, Supplement* **208** (Oct.,
 1111 2013) 19, [arXiv:1212.5226 \[astro-ph.CO\]](#).
- 1112 [17] **Planck** Collaboration, P. Ade *et al.*, “Planck 2015 results. XIII.
 1113 Cosmological parameters,” [arXiv:1502.01589 \[astro-ph.CO\]](#).
- 1114 [18] A. Martin, W. Stirling, R. Thorne, and G. Watt, “Parton distributions for
 1115 the LHC,” *Eur.Phys.J.* **C63** (2009) 189–285, [arXiv:0901.0002 \[hep-ph\]](#).
- 1116 [19] P. M. Nadolsky, H.-L. Lai, Q.-H. Cao, J. Huston, J. Pumplin, *et al.*,
 1117 “Implications of CTEQ global analysis for collider observables,” *Phys.Rev.*
 1118 **D78** (2008) 013004, [arXiv:0802.0007 \[hep-ph\]](#).
- 1119

- 1120 [20] R. D. Ball, L. Del Debbio, S. Forte, A. Guffanti, J. I. Latorre, *et al.*, “A first
1121 unbiased global NLO determination of parton distributions and their
1122 uncertainties,” *Nucl.Phys.* **B838** (2010) 136–206, arXiv:1002.4407
1123 [hep-ph].
- 1124 [21] M. E. Peskin and D. V. Schroeder, *An introduction to quantum field theory*.
1125 Advanced book program. Westview Press Reading (Mass.), Boulder (Colo.),
1126 1995. <http://opac.inria.fr/record=b1131978>. Autre tirage : 1997.

Contents

1128 1 The CMS experiment at LHC	3
1129 1.1 The Large Hadron Collider	3
1130 1.1.1 Injector chain	4
1131 1.1.2 Main ring	6
1132 1.1.3 Run 1	9
1133 1.1.4 Other experiments at LHC	10
1134 1.2 The Compact Muon Solenoid (CMS) experiment	12
1135 1.2.1 Coordinate system	15
1136 1.2.2 Magnet	17
1137 1.2.3 Tracker system	18
1138 1.2.4 Electromagnetic calorimeter	20
1139 1.2.5 Hadronic Calorimeter	20
1140 1.2.6 Muon chambers	23
1141 1.2.7 Trigger	25
1142 1.3 Object reconstruction	27
1143 1.3.1 Track and vertex reconstruction	27
1144 1.3.2 Particle Flow (PF) algorithm	27
1145 1.3.3 Electron reconstruction	28
1146 1.3.4 Muon reconstruction	28
1147 1.3.5 Jet reconstruction	28
1148 2 The Standard Model	31
1149 2.1 Fields, symmetries and interactions	32
1150 2.2 Quantum fields and particles	34
1151 2.2.1 The mass problem	36
1152 2.2.2 Spontaneous Symmetry Breaking	37
1153 2.2.3 Englert-Brout-Higgs mechanism	38
1154 2.3 Top production at LHC	39
1155 2.3.1 Pair production	39
1156 2.3.2 Single t production	40
1157 2.3.3 Decay channels	40
1158 2.3.4 Top properties	40

1159	2.4	Higgs production at LHC	40
1160	2.4.1	Decay channels	41
1161	2.4.2	Higgs properties	41
1162	2.5	Hierarchy problem and other limitations	41
1163	3	VLQ models	45
1164	3.1	Motivation	45
1165	3.2	Generic Formulation	45
1166	3.2.1	Production modes	45
1167	3.2.2	Decay modes	46
1168	3.3	Fesability study for a search of a T at LHC at 8 TeV	46
1169	3.3.1	Stragey for the full hadronic final state	46
1170	3.3.2	Event selection	46
1171	3.3.3	Results	46
1172	4	MC event generation	47
1173	4.1	Mote-Carlo simulations	47
1174	4.1.1	Parton simulation	48
1175	4.1.2	Hadron simulation	50
1176	4.1.3	Detector simulation	50
1177	4.2	Tools	50
1178	4.2.1	Matrix-element generators	50
1179	4.2.2	Hadron generators	50
1180	4.3	Validation on data	50
1181	5	Single VLQ search	53
1182	5.1	Analysis Strategy	53
1183	5.2	Datasets	53
1184	5.3	Event selection	53
1185	5.3.1	Event processing	53
1186	5.3.2	Basic selection	53
1187	5.3.3	T' reconstruction with a χ^2 sorting algorithm	54
1188	5.3.4	Selection based on reconstructed objects	54
1189	5.3.5	Efficiencies	54
1190	5.4	Background estimation from data	54
1191	5.4.1	Known difficulties and tried methods	54
1192	5.4.2	Method	55
1193	5.4.3	Validation	55
1194	5.5	Systematics	55
1195	5.6	Results	55